A preliminary Survey on Wavefunction Overlaps in (L)APW and Wannier function Bases

Dara Goldar

December 2016

SPECIALIZATION PROJECT

Faculty of Natural Sciences and Technology
Department of Physics

Norwegian University of Science and Technology

Supervisor: Trond Brudevoll, Asta Storeboe (Researchers at Norwegian Defence Research Establishment)
Faculty supervisor: Jon Andreas Stvneng (Assoc. Prof. at the Department of Physics)

Abstract

During the work with this specialization project, expressions for the overlap integral between eigenfunctions are derived in the LAPW and Maximally localized Wannier function bases. These expressions must be suitable for numerical integration over the Brillouin zone so that scattering rates for any particular scattering mechanism may be obtained in the context of carrier simulations using the Monte Carlo method. While the expression found for the LAPW basis is considered satisfactory with respect to the above requirements, more work is needed to arrive at a sufficiently good Wannier overlap expression. Furthermore, eigenfunctions and bandstructures have been obtained for semiconductor materials Gallium arsenide, Silicon and Mercury cadmium telluride in the local density approximation, using the softwares Wien2k, Wien2Wannier and Wannier90. For Gallium arsenide and Silicon, band edge properties are discussed in light of the nature of the bandgap and spin-orbit coupling. For Mercury cadmium telluride, the validity of the local density approximation has been investigated. The results show good agreement with data from literature, but improvements can be made: instead of the local density approximation model currently used, an improved exchange potential mbJ+U should be used. In addition, Vegard's law has been used to model the crystal structure of HgCdTe, and this should be replaced by a supercell model combined with so-called unfolding of the bandstructure.

Table of Contents

Abstract i

Table of Contents iv

1 Introduction 1

2 Theory 5
- 2.1 Scattering rates . . . 5
- 2.2 Density Functional theory . . . 7
  - 2.2.1 Kohn - Sham equations & Self-consistent cycle . . . 7
  - 2.2.2 Spin-polarized systems . . . 8
  - 2.2.3 LDA+U . . . 9
- 2.3 Full potential Augmented plane-wave method . . . 10
  - 2.3.1 Partitioning of the unit cell . . . 10
  - 2.3.2 LAPW+lo and APW+lo . . . 12
- 2.4 Wannier functions . . . 13
  - 2.4.1 Maximally localized Wannier functions . . . 14

3 Scattering rates in LAPW and Wannier basis 17
- 3.1 LAPW overlap . . . 18
  - 3.1.1 Region I . . . 19
  - 3.1.2 Region II . . . 20
  - 3.1.3 Total overlap . . . 21
- 3.2 Wannier overlap . . . 22

4 Results and discussion 25
- 4.1 GaAs . . . 25
- 4.2 Silicon . . . 30
- 4.3 HgCdTe . . . 33

5 Conclusion and future work 37

Bibliography **39**

Chapter 1

Introduction

Computational electronics is increasingly playing an important role in explaining physical phenomena in semiconductor devices. The behaviour of these electronic devices is becoming ever more complex as the size of electronic components enter into the nanometer regime. At the nanometer scale, new physical fenomena only occurring at the shortest scales must be taken into consideration. From an electronics engineer's point of view, the processes involved in manufacturing electronics components in the nanometer regime are complex and time-consuming, so a trial-and-error approach may turn out to be impossible simply because it's too costly. Here, computational electronics offers the electronics engineer insight into component behaviour at a significantly lower cost. It also allows the engineer to simulate hypothetical devices that presently are not technologically possible to manufacture. Finally, device simulations allow the engineer to observe aspects of device behaviour that are impossible to measure in experiments with real electronics devices. Electronics device simulations should not only provide a sufficiently sophisticated model, but preferably do so at minimal computational cost and within a reasonable time frame. [1]

This specialization project deals with the generation of bandstructures and eigenfunctions for semiconductor materials Mercury Cadmium telluride (HgCdTe), Gallium arsenide (GaAs) and Silicon (Si) from first-principles methods. The work done here is part of a larger project aiming at providing a 'general purpose' Monte Carlo program for charge carrier transport. It should be 'general purpose' in the sense that different materials may be simulated equally well with little effort needed to go from one material to another. Since no actual transport simulations are discussed in this report, the Monte Carlo method will only be discussed in light of the input data it takes. At the time of writing, the Monte Carlo program accepts analytical bandstructures as well as tabulated bandstructures from first principles programs. The analytical band model has a well-defined mathematical representation while the tabulated model is a discrete representation of the bandstructure. In previous work done by Karlsen, Selvaag and Bergslid, Monte Carlo simulations using scattering rates calculated from the $\boldsymbol{k} \cdot \boldsymbol{p}$ method [2] as well as full-band data acquired by first-principles program ABINIT have been presented [3] [4] [5] [6]. While both the $\boldsymbol{k} \cdot \boldsymbol{p}$

method and a first-principles tabulated representation of the bandstructure have been used, eigenfunctions have until now only been calculated using the $\boldsymbol{k} \cdot \boldsymbol{p}$ method. The next step will be to run simulations not only based on a first-principles bandstructure, but also using first-principles generated eigenfunctions. To this end, bandstructures and eigenfunctions have been generated within the full-potential LAPW method from Wien2k[7], and may hopefully be run on the Monte Carlo program in the near future.

In addition to simulating carrier transport using the LAPW representation, it is possible to use a real-space basis known as the Maximally localized Wannier representation (MLWFs). There are a number of advantages associated with the use of a MLWF representation compared to the original LAPW basis which Wien2k uses. First of all, the current Monte Carlo program uses bandstructures and potentially eigenfunctions from external ab-initio programs, e.g ABINIT or WIEN2k. Many different ab-initio programs exist today, each one potentially based on a particular basis. A standardization, where one does not need to worry about the basis in which input parameters are represented, will obviously make the transport program more attractive. One simply converts a specific ab-initio representation into a standardised representation used for the Monte Carlo program. In order to implement such a standardization one needs a general algorithm able to change the representation found in most ab-initio programs to the standardized functions used. Indeed, such an algorithm has been developed by Nicola Mazari, Ivo Souza and David Vanderbilt that iteratively transforms a set of Bloch orbitals obtained from a first-principles calculation into a set of Maximally localized Wannier functions. This algorithm works without regard to the particular first-principle calculation technique adopted or the basis set, and therefore satisfies the requirements needed for a standardization of the Monte Carlo program [8]. Secondly, the Wannier representation is well suited for quantum transport. This is because the MLWF offer a compact representation, yielding much simplified tight-binding like operations related to bandstructure and transport calculations. Currently, bandstructure and transport are done in series, but in simulation of very small devices, bandstructures are recalculated in parallell with the transport simulation to account for internal redistribution of charge [1]. This represents a formidable computational task and is done at a lower computational cost in a tight-binding like representation [8]. A final advantage of the Wannier representation is linear scaling. Linear scaling methods are electronic structure calculation methods where the computational cost increases only linearly with the size of the system. One uses results from electronic-structure calculations on smaller systems to model larger systems. Due to the above reasons, it is sometimes expedient to post-process the Wien2k data using the Wien2k-interface Wien2Wannier [4] and the program Wannier90 [4] [9], carrying eigenfunctions in the LAPW over to a Maximally localized Wannier basis. It should be emphasized that Wannier functions are to be used only when they are beneficial in their own right for the particular problem of interest. It is in fact intended that both the LAPW method and Wannier representation are available as representations used in the Monte Carlo simulations.

In the calculation of scattering rates, the eigenfunctions, whether they are expressed through MLWFs or through the LAPW method, mainfest themselves through overlap integrals between initial and final scattering states of the charge carrier undergoing scattering. By

including eigenfunctions generated from first-principles calculations, it must be possible to integrate over the eigenfunctions to obtain overlaps relevant for a given scattering mechanism. Therefore, expressions suitable for numerical integration over the discrete Brillouin zone are needed to determine the scattering rate for each individual scattering mechanism included in the Monte Carlo simulation.

The work done specifically in this specialization project may be summarized as follows:

- Installing the ab initio program Wien2k, Wannier90 and the graphical tool XCrySDen.
- Learning to use Wien2k, Wien2Wannier and the Monte Carlo transport program.
- Obtaining numerically suitable expressons for scattering rates in the LAPW method and for Wannier functions, respectively.
- Using Wien2k to calculate bandstructures and eigenfunctions for MCT, GaAs and Si.
- Generating and plotting Maximally localized Wannier functions (MLWFs) for GaAs and Si.

There are already a number of transport packages simulating carrier behaviour which are based on first-principles calculations in the LAPW method and Wannier basis, respectively, and much time on this project has been spent understanding these methods to determine whether they have potential application for the Monte Carlo program. Ambrosch-Draxl et al. (2006) presents a scheme for calculating optical properties using the full-potential LAPW method [10]. The optical properties are discussed within the random-phase approximation [11]. Since Ambrosch-Draxl et al. are interested in the dielectric constant, they develop an expression involving momentum matrix elements in the LAPW basis. Another package called woptic, developed by Assmann et al. (2015) calculates the optical conductivity in a basis of Maximally localized Wannier functions. Within the framework of dynamical-mean-field-theory [12], the optical conductivity is given as a Brillouin-zone sum involving dipole matrix elements expressed in terms of Wannier functions [13]. Although the packages offered by Ambrosch-Draxl et al. and Assmann et al. evaluate overlaps in the LAPW and Wannier basis respectively, these overlaps differ from the overlaps used in the Monte Carlo program. First, they involve dipole matrix elements rather than overlap matrix elements; and second, these overlaps are restricted to initial and final wavevectors being the same. In other words, we are interested in the matrix elements $\langle n'\boldsymbol{k'}|n\boldsymbol{k}\rangle$ but Ambrosch-Draxl et al. (2006) and Assmann et al. (2015) present schemes involving $\langle n'\boldsymbol{k'}|\,\boldsymbol{p}\,|n\boldsymbol{k}\rangle$ where $\boldsymbol{p}$ is the momentum operator and n, n' are band indices.

Two other interesting schemes, based on solving the Boltzmann transport equations (BTEs) in the relaxation time approximation are available [14]. In the context of Boltzmann transport in the relaxation time approximation, the relaxation time τ represents the contribution to transport from scattering, and there is indeed a formal connection [2]. The first of the two schemes, a code for simulating electron behaviour, is presented by Madsen et al. (2006) and is called BoltzTraP [15]. BoltzTraP is a code for calculating transport

quantities such as the semi-classic Seebeck and Hall coefficients in the LAPW method. Bandstructures are Fourier expanded and an analytical bandstructure obtained. This analytical expression allows one to easily calculate bandstructure-dependend quantities such as derivatives. Once analytical band expressions are obtained, the Botzmann transport equations (BTEs) are solved in the relaxation time approximation. In its early days, the code assumed constant relaxation time τ , but new versions allow for an energy-dependent $\tau\epsilon$ model [16]. Another code, BoltzWann, is presented by G. Pizzi et al. (2014). Also based on BTEs within the relaxation time approximations, BoltzWann calculates bandstructure dependent quantities using the Wannier representation instead of the LAPW method. Analytical bandstructures are obtained using Wannier interpolation [8], making bandstructure-dependent quantities easily accessible. While BoltzTrap only allows for an energy-dependent relaxation time model, BoltzWann on the other hand is able to use any model for the relaxation time, even those based on first-principles calculations [17]. While the methods described above differ from Monte Carlo by being based on the Boltzmann transport equation in the relaxation time approximation, the interpolation schemes used in BoltzWann and BoltzTrap may be of interest since they offer a way of saving data on a coarse mesh and interpolate without significant loss of precision. Two possible applications of interest have been found for the MC program: First, when dealing with the overlap between states of different wavenumber k and k', the amount of data needed to tabulate the overlaps on a fine mesh is impractical, and Fourier interpolation or Wannier interpolation may be helpful. Second, Bergslid (2013) reported in his work a ripple effect in the Monte Carlo program with the current BZ integration method [6]. Currently, the Gilat-Raubenheimer method is used for BZ integration, and in this context the interpolation scheme used is by Fischetti & Laux [18] [19]. To prevent the ripple effect reported by Bergslid, a band interpolation scheme developed by E. Pickett et al. (1988) may be of interest [20].

This report is organized as follows: Chapter 2 presents scattering rates within first order pertubation theory, density functional theory, and the bases LAPW and Wannier functions. In chapter 3, expressions for overlap integrals in the LAPW method and Wannier representation are derived. In chapter 4, results from simulations with Wien2k and Wannier90 are presented and discussed for GaAs, Silicon and HgCdTe, respectively. Finally, in Chapter 5, conclusions are drawn based on the simulations and finally future work discussed.

Chapter 2

Theory

2.1 Scattering rates

A number of different scattering mechanisms contribute to the transport of electrons, some of them being

- Acoustic deformation potential phonon scattering
- Acoustic piezoelectric phonon scattering
- Polar optical phonon scattering
- Nonpolar optical phonon scattering
- Ionized impurity scattering
- Neutral impurity scattering
- Carrier-carrier scattering
- Alloy scattering

Depending on material, temperature and carrier concentration, some of the mechanisms will play a negligible role in carrier transport and may be omitted while others will dominate. The scattering rates are usually given by first order time-dependent perturbation theory. The probability of transition per unit time from one energy-eigenstate to another for a particular scattering mechanism is according to Fermi's Golden Rule given as

$$P^m_{nn'}(\boldsymbol{k}, \boldsymbol{k'}) = \frac{2\pi}{\hbar}\left|M^m_{nn'}(\boldsymbol{k}, \boldsymbol{k'})\right|^2 \delta\big(E_n(\boldsymbol{k}) + \Delta E^m(\boldsymbol{k}, \boldsymbol{k'}) - E'_n(\boldsymbol{k})\big) \tag{2.1}$$

The initial state is labelled by band index n and wavenumber $\boldsymbol{k}$, the final state by band index n' and wavenumber $\boldsymbol{k'}$. m denotes the particular scattering mechanism at play. $M^m_{nn'}(\boldsymbol{k}, \boldsymbol{k'})$ represents the interaction matrix element for the transition, depending on the

initial and final state as well as the perturbed potential. ΔE^m is the energy added to the carrier undergoing scattering. Finally, $E_n(\boldsymbol{k})$ is the dispersion relation for band n. While the delta-function ensures energy conservation, momentum conservation is maintained through the interaction matrix element. However, in the context of Bloch states (crystals), the momentum conservation holds only up to a reciprocal lattice vector: $\boldsymbol{k} - \boldsymbol{k'} + \boldsymbol{q} = \boldsymbol{K}$. Here, $\boldsymbol{q}$ denotes a Fourier component of the perturbed potential. In the case of carrier-phonon scattering for example, it is interpreted as $\pm$ the phonon momentum, depending on whether the phonon is absorbed or emitted, respectively. $\boldsymbol{K}$ represents a reciprocal lattice vector. If zero, the scattering process is called normal, otherwise one calls it an Umklapp process.

It is often convenient to decompose the interaction matrix element into a part involving the scattering interaction and another the overlap between the initial and final state

$$\left|M^m_{nn'}(\boldsymbol{k}, \boldsymbol{k'})\right|^2 = \left|C^m_{nn'}(\boldsymbol{k}, \boldsymbol{k'})\right|^2 G_{nn'}(\boldsymbol{k}, \boldsymbol{k'}) \tag{2.2}$$

The overlap factor $G_{nn'}(\boldsymbol{k}, \boldsymbol{k'})$ is taken over the unit cell and only involves the cell-periodic part of the initial and final Bloch wave. The decomposition in (2.2) is formal, i.e $\left|C^m_{nn'}(\boldsymbol{k}, \boldsymbol{k'})\right|^2 = \frac{\left|M^m_{nn'}(\boldsymbol{k}, \boldsymbol{k'})\right|^2}{G_{nn'}(\boldsymbol{k}, \boldsymbol{k'})}$. In practice however, one often approximates this relation by assuming the interaction to be constant over the unit cell (see for example chapter 6.5 of J. Singh, *Electronic and optoelectronic properties of semiconductor structures* [2]) [21]. The overlap factor reads

$$G_{nn'}(\boldsymbol{k}, \boldsymbol{k'}) = \Big| \int_{\text{u.c}} d^3 r u^*_{n'\boldsymbol{k'}} u_{n\boldsymbol{k}} e^{i\boldsymbol{K}\cdot\boldsymbol{r}} \Big|^2 \tag{2.3}$$

where $\boldsymbol{K}$ is again a reciprocal lattice vector and $u_{n\boldsymbol{k}}$ is the cell-periodic part of the Bloch state and the integral runs over the unit cell. (2.3) in its current form does not take spin-flipping into account. The initial and final states for a scattering process are generally described with a spin index as well, so in order to take this into account, we average over initial spin states and sum over final spin states.

$$G_{nn'}(\boldsymbol{k}, \boldsymbol{k'}) = \frac{1}{2} \sum_{\sigma} \sum_{\sigma'} \Big| \int_{\text{u.c}} d^3 r u^*_{n'\boldsymbol{k'}\sigma'} u_{n\boldsymbol{k}\sigma} e^{i\boldsymbol{K}\cdot\boldsymbol{r}} \Big|^2 \tag{2.4}$$

where σ and σ' each denote either spin up or spin down, and the sum runs over these two spin orientations.

If the scattering interaction $\left|C^m_{nn'}(\boldsymbol{k}, \boldsymbol{k'})\right|^2$ for a particular scattering mechanism is known, all that remains to determine the scattering rate is $G_{nn'}(\boldsymbol{k}, \boldsymbol{k'})$. The interaction matrix element $\left|C^m_{nn'}(\boldsymbol{k}, \boldsymbol{k'})\right|^2$ may be found for a number of scattering mechanism from Brudevoll et al. (1990) and Ridley B. K, *Quantum Processes in Semiconductors* [22] [14].

2.2 Density Functional theory

2.2.1 Kohn - Sham equations & Self-consistent cycle

The Hohenberg-Kohn theorem states that for a given system, the total energy may be given as a functional of the ground state electron density. Furthermore, this ground state electron density minimizes the total energy functional. Both electron interactions and external potentials are taken into account. For our purposes, the system denotes the crystal of interest and the external potential is the Coulomb potential from the nuclei crystal. While the original theorems applied to non-spin-polarized systems, it has later been generalized to take spin-polarization into account. Nonetheless, we will present the non-spin-polarized version first:

$$E = E[\rho] \tag{2.5}$$

Even though the Hohenberg-Kohn theorem guarantees that an energy potential exists, it does not provide any model for the energy functional itself. For density functional theory to be useful, it is vital that the model used for the functional is sufficiently accurate. The functional may be decomposed into a set of terms corresponding to different kinds of energy contributions

$$E = E[\rho] = T_s[\rho] + E_{ei}[\rho] + E_H[\rho] + E_{ii}[\rho] + E_{xc}[\rho] \tag{2.6}$$

$T_s[\rho]$ is the single particle kinetic energy; $E_{ei}[\rho]$ is the energy due to the Coulomb interaction between electrons and nuclei; $E_{ii}[\rho]$ comes from nucleon-nuclei interactions and the electron-electron interaction is decomposed into $E_H[\rho]$ and $E_{xc}[\rho]$

$$E_H[\rho] = \frac{e^2}{2} \int d^3r d^3r' \frac{\rho(\boldsymbol{r})\rho(\boldsymbol{r'}}{|\boldsymbol{r} - \boldsymbol{r'}|} \tag{2.7}$$

$$E_H[\rho] = \int d^3r \rho(\boldsymbol{r}) \epsilon_{xc}(\rho(\boldsymbol{r})) \tag{2.8}$$

The Hartree energy is due to the Coulomb-repulsion between electrons, and its analytical expression is given exactly. The exchange-correlation term on the other hand is not known and must be approximated by defining $E_H[\rho]$ appropriately. The expression in (2.8) is in the local density approximation (LDA) since $\epsilon_{xc}[\rho(\boldsymbol{r})]$ is a function only local in the density. Another common model, the generalized gradient approximations (GGAs) includes the local density as well as the local gradient. Several other models exist as well, see for example [ref].

In order to determine the ground state energy and ground state density, we write the total density in terms of single particle densities

$$\rho(\boldsymbol{r}) = \sum_i^N \phi_i^*(\boldsymbol{r})\phi_i(\boldsymbol{r}) \tag{2.9}$$

and invoke the Variational principle to find the ground state energy with respect to $\rho(\boldsymbol{r})$. Doing so yields the Kohn-Sham equations as shown by W. Kohn and L. J. Sham in 1965 [23]

$$V_{KS}\phi_i(\boldsymbol{r}) = \big(T + V_{ei}(\boldsymbol{r}) + V_H(\boldsymbol{r}) + V_{xc}(\boldsymbol{r})\big)\phi_i(\boldsymbol{r}) = \epsilon_i\phi_i(\boldsymbol{r}) \tag{2.10}$$

$$\rho(\boldsymbol{r}) = \sum_i^N \phi_i(\boldsymbol{r})\phi_i^*(\boldsymbol{r}) \tag{2.11}$$

where T is the single-particle kinetic energy operator, V_{ei} denotes the Coulomb potential operator for orbital $\phi_i(\boldsymbol{r})$, V_H is due to the Coulomb interaction between electrons, V_{xc} is the exchange-correlation potential and finally ϵ_i is the Kohn-Sham eigenvalue corresponding to the Kohn-Sham orbital $\phi_i(\boldsymbol{r})$. $V_H(\boldsymbol{r})$ and $V_{xc}(\boldsymbol{r})$ are explicitly given by

$$V_H(\boldsymbol{r}) = e^2 \int d^3\boldsymbol{r'} \frac{\rho(\boldsymbol{r'})}{|\boldsymbol{r} - \boldsymbol{r'}|} \tag{2.12}$$

$$V_{xc}(\boldsymbol{r}) = \frac{\delta E_{xc}[\rho]}{\delta\rho(\boldsymbol{r})} \tag{2.13}$$

In (2.11), the sum runs over the N electrons in the crystal. Finally, the total energy is related to the Kohn-Sham eigenvalues through

$$E = \sum_i^N \epsilon_i - E_H[\rho] + E_{xc}[\rho - \int \frac{\delta E_{xc}[\rho]}{\delta\rho}\rho(\boldsymbol{r})d\boldsymbol{r} \tag{2.14}$$

While (2.10) provides an equation for the ground state density and thereby the total ground state energy of the system, the Kohn-Sham equations are self-consistent equations. In order to solve the equations, the electron density is needed to determine the Hartree and exchange-correlation potentials. At the same time, we are solving the Kohn-Sham equations in order to determine the same electron density. In practice, the Kohn-Sham equations are solved self-consistently by making an initial guess for the density and then solve for the electron density repeatedly until convergence.

2.2.2 Spin-polarized systems

If an external magnetic field is applied to an electronic system, this will modify the charge density due to the electron's and its spin's interaction with the external magnetic field. This generally gives rise to a preferred spin orientation for the electrons and we therefore call such a system a spin-polarized system. While the magnetization may generally vary in magnitude and direction from one point in space to another (a vector field), it is reduced to a scalar field in the case of collinear magnetization, i.e where the magnetization only varies along one direction. The two relevant scalar fields read

$$\rho(\boldsymbol{r}) = \rho_\uparrow(\boldsymbol{r}) + \rho_\downarrow(\boldsymbol{r}) \tag{2.15}$$

$$m(\boldsymbol{r}) = \rho_\uparrow(\boldsymbol{r}) - \rho_\downarrow(\boldsymbol{r}) \tag{2.16}$$

The generalized Hohenberg-Kohn theorem then postulates a ground state energy. This energy is acquired by invoking the variational principle on an energy functional which now depends on the spin densities in (2.15) and (2.16) [24]

$$E = E[\rho_\uparrow, \rho_\downarrow] \tag{2.17}$$

We proceed to segment into different energy contributions, analogous to the decomposition made in (2.6) and invoke the variational principle to get the Kohn-Sham orbitals for the spin-polarized case

$$V_{KS}\phi_{i,\boldsymbol{\sigma}}(\boldsymbol{r}) = \big[T + V_{ei}(\boldsymbol{r}) + V_H(\boldsymbol{r}) + V_{xc,\boldsymbol{\sigma}}(\boldsymbol{r})\big]\phi_{i,\boldsymbol{\sigma}}(\boldsymbol{r}) = \epsilon_{i,\boldsymbol{\sigma}}\phi_{i,\boldsymbol{\sigma}}(\boldsymbol{r}) \tag{2.18}$$

$$\rho_\sigma(\boldsymbol{r}) = \sum_i^N \phi_{i,\sigma}(\boldsymbol{r})\phi^*_{i,\sigma}(\boldsymbol{r}) \tag{2.19}$$

where a new index $\boldsymbol{\sigma}$ corresponding to $\uparrow$ and $\downarrow$ has been introduced. Except for the exchange-correlation potential, given by

$$V_{xc,\boldsymbol{\sigma}}(\boldsymbol{r}) = \frac{\delta E_{xc}[\rho_\uparrow, \rho_\downarrow]}{\delta \rho_\sigma(\boldsymbol{r})} \tag{2.20}$$

all the other terms are defined as in (2.10). In the spin-polarized case, we are instead dealing with two spin electron densities instead of one, so there are two sets of Kohn-Sham equations.

2.2.3 LDA+U

A challenge with the local (spin) density approximation is the fact that it does not properly capture the contribution from strongly correlated electron states since it assumes local exchange-correlation. LDA+U is an attempt to better model these strongly correlated states, typically f and d orbitals [25], using the Hubbard model [26]. The modified energy functional in LDA+U is given by

$$E_{LDA+U}[\rho(\boldsymbol{r})] = E_{LDA}[\rho(\boldsymbol{r})] + E_{Hub} - E_{dc} \tag{2.21}$$

where $E_{LDA}[\rho(\boldsymbol{r})]$ is the original energy functional (2.6), E_{Hub} is the contribution to the energy functional from strongly correlated electron states through a Hubbard model, and since E_{LDA} already takes the *local* exchange-correlation into account, a third term E_{dc} is added to correct for the double counting. E_{Hub} is given by

$$E_{Hub}[\{n_m^{I\sigma}, n_{m'}^{I\sigma'}\}] = \frac{U^I}{2} \sum_{m,\sigma \neq m'\sigma'} n_m^{I\sigma} n_{m'}^{I\sigma'} \tag{2.22}$$

E_{dc} is however not uniquely defined as there are more ways of making the double-counting correction. Different schemes exist, but the two most popular choices are the so-called around mean-field (AMF) [27] and "fully localized limit" (FLL) [28].

2.3 Full potential Augmented plane-wave method

The (linearized) augmented plane-wave method ((L)APW) is a popular method in the context of electronic structure calculations of crystals. The method is a procedure for solving the Kohn-Sham equations for the total energy, ground state density, eigenfunctions and eigenvalues of a many-electron system[29] - the main computational task in the local density spin approximation (LSDA) of density functional theory. The method is especially well-suited for solving the KS equations because the basis has been adapted specifically for electronic structure calculations in the context of crystals.

Slater formulated the Augmented Plane Wave (APW) method in 1937. In the original method the basis consisted of energy-dependent basis functions, and this energy-dependence yields a non-linear eigenproblem which is solved iteratively at great computation cost [refreence]. If one however fixes the energy at a so-called linearization energy E_l, a different eigenstate with its associated eigenenergy will be poorly described. In the LAPW method, one fixes the energy in order to linearize the eigenproblem, but compensates for the loss in flexibility by modifying the basis set. This allows one to better account for energies differing from the linearization energy. The linearization itself is typically performed in two ways: 1) In the LAPW method the atomic orbital like functions from region (I) are matched in value and slope at the sphere boundary with that of plane-waves from region (II). 2) In the APW plus local orbitals method (APW+lo) atomic orbital-like functions are matched with plane-waves *only* in value at the sphere boundary, resulting in kinks at the sphere boundary for the basis functions.

Starting with a general expression to convey the basic idea behind APW, some of the differences between the two linearized methods mentioned above will be presented after.

2.3.1 Partitioning of the unit cell

In the APW method the unit cell is separated into two regions: a region, denoted by I, of atomic spheres centered around real-space atomic points where the potential is assumed to be spherically symmetric, and an interstitial region, denoted by II.

The basis set is defined differently for the two regions. In region I the basis is expressed as a linear combination of radial functions multiplied by spherical harmonics. These are centered inside their respective sphere, denoted by β, so region I is generally a fragmented region of spheres around each and every atom in the unit cell. Focusing our attention on a specific sphere, but keeping in mind that contributions from all spheres must be added, we write

$$\psi^{\sigma}_{\boldsymbol{k}}(\boldsymbol{r}) = \sum_{lm} \left[a^{\beta\sigma}_{\boldsymbol{k},lm} u^{\beta\sigma}_{1,l}(r_\beta, E_l) + b^{\beta\sigma}_{\boldsymbol{k},lm} \dot{u}^{\beta\sigma}_{1,l}(r_\beta, E_l) + c^{\beta\sigma}_{\boldsymbol{k},lm} u^{\beta\sigma}_{2,l}(r_\beta)\right] Y_{lm}(\boldsymbol{r}_\beta, E_l) \tag{2.23}$$

Here, u_1, $\dot{u}_1$ and u_2 are radial functions depending on the spin projection σ (for spin polarized calculations); energy E_l; orbital quantum number l; and finally the radius $r_\beta =$

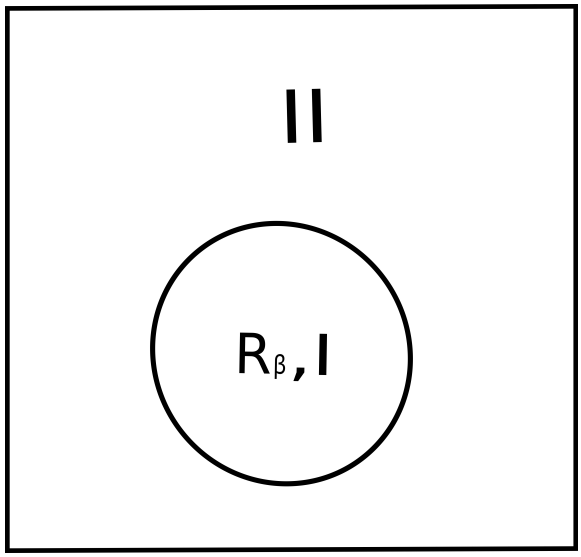

Figure 2.1: *Partitioning of the unit cell into two regions: atomic spheres centered around $\boldsymbol{R}_\beta$ in region I and an interstital part, region II. There may generally be more than one sphere making up region I, each sphere corresponding to a nucleus in the unit cell.*

$|\boldsymbol{r} - \boldsymbol{R_\beta}|$ which is defined according to the center of the sphere β (see figure 2.1). In other words, β does not denote the radius from a global origin.

The radial functions and the coefficients are defined according to which scheme is being used, for our purposes either LAPW+lo or APW+lo. Generally, the radial functions are associated with radial solutions to the Schroedinger equation at a given energy E_l and also the energy derivative $\frac{du}{dE}$ evaluated at E_l [30]. The radial functions and basis coefficients are explained in detail for both LAPW+lo and APW+lo in the next section.

For region II, we expand our basis in terms of plane-waves

$$\psi^\sigma_{\boldsymbol{k}}(\boldsymbol{r}) = \frac{1}{\sqrt{V}} \sum_{\boldsymbol{G}} C^\sigma_{\boldsymbol{k}} e^{i(\boldsymbol{k}+\boldsymbol{G})\cdot\boldsymbol{r}} \tag{2.24}$$

The basis function is entirely defined in terms of the expansion coefficients $C^\sigma_{\boldsymbol{k}}$ since we have continuity conditions for the wavefunction on the sphere boundary. $a^{\beta\sigma}_{\boldsymbol{k},lm}, b^{\beta\sigma}_{\boldsymbol{k},lm}, c^{\beta\sigma}_{\boldsymbol{k},lm}$ are all functions of $C^\sigma_{\boldsymbol{k}}$ defined in terms of the continuity condition invoked between region (I) and (II). Even though the wavefunction for region I has an index β associated with the particular atomic site located at $\boldsymbol{R_\beta}$, region II has no such indices since it does not belong to a particular atomic site. Finally, the band index has been omitted from the state $\psi^\sigma_{\boldsymbol{k}}(\boldsymbol{r})$ and associated expansion coefficients $C^\sigma_{\boldsymbol{k}}, a^{\beta\sigma}_{\boldsymbol{k},lm}, b^{\beta\sigma}_{\boldsymbol{k},lm}, c^{\beta\sigma}_{\boldsymbol{k},lm}$ for simplicity.

The total wavefunction is expanded in this augmented plane-wave basis (with band index reintroduced in the basis functions)

$$\Psi_{\boldsymbol{k}}^{\sigma} = \sum_{n} c_n \psi_{\boldsymbol{k}_n} \tag{2.25}$$

Finally, the potential for both schemes (LAPW+lo or APW+lo) is expanded according to

$$V(\boldsymbol{r}) = \begin{cases} \sum_{LM} V_{LM}(r) Y_{LM}(\hat{\boldsymbol{r}}) & \text{region I} \\ \sum_{K} V_K(r) e^{i\boldsymbol{K}\cdot\boldsymbol{r}} & \text{region II} \end{cases} \tag{2.26}$$

where K denotes a reciprocal lattice vector and Y_{LM} again corresponds to spherical harmonics.

2.3.2 LAPW+lo and APW+lo

As mentioned initially in this section, different schemes for the definition of the radial functions and continuity conditions in (2.23) exist. Starting with the LAPW method, the wavefunction for region I is given (spin and band index omitted for simplicity)

$$\psi_{\boldsymbol{k}_n}(\boldsymbol{r}) = \sum_{lm} \left[A_{lm,\boldsymbol{k}_n} u_l(r) + B_{lm,\boldsymbol{k}_n} \dot{u}_l(r) \right] Y_{lm}(\hat{\boldsymbol{r}}) \tag{2.27}$$

where the expansion coefficients not only depend on sum parameters l and m, but also the wavevector $\boldsymbol{k}_n$, and $\dot{u}_l(r, E) = \frac{du}{dE}\big|_l$. To obtain additional flexibility and ensure orthogonality, additional basis terms may be added in what is called the local orbital extension

$$\psi^{LO}(\boldsymbol{r}) = \sum_{lm} \left[A_{lm} u_l(r, E_{1,l}) + B_{lm} \dot{u}_l(r, E_{1,l}) + C_{lm} u_l(r, E_{2,l}) \right] Y_{lm}(\hat{\boldsymbol{r}}) \tag{2.28}$$

These additional terms consist of one energy derivative and a linear combinations of radial functions evaluated at two different linearization energies. By demanding normalization and zero value on the boundary between region I and II, the coefficients are determined.

We may similarly construct a basis set in the APW+lo basis

$$\psi_{\boldsymbol{k}_n}(\boldsymbol{r}) = \sum_{lm} \left[A_{lm,\boldsymbol{k}_n} u_l(r) + \phi_{lm}^{lo} \right] Y_{lm}(\hat{\boldsymbol{r}}) \tag{2.29}$$

with the local orbital extension

$$\phi_{lm}^{lo} = B_{lm} u_l(r) + C_{lm,\boldsymbol{k}_n} \dot{u}_l(r) \big] Y_{lm}(\hat{\boldsymbol{r}}) \tag{2.30}$$

Although this looks similar to the LAPW method excluding local orbitals, there are some significant differences: First, coefficients B_{lm} and C_{lm} do not depend on $\boldsymbol{k}_n$, they are determined by $\phi^{lo} = 0$ at the boundary between the two regions and also normalization. Second, there are no restrictions on the wavefunction derivate at the sphere boundary (the value of $\psi_{\boldsymbol{k}_n}$ between the two regions must still match). Finally, the linear combinations

including $\dot{u}_l(r)$ need only enter for $l \leq 3$, meaning that most of the terms in 2.29 only include u_l, and are easily constructed compared with LAPW+lo [31]. In fact, Madsen et al. (2001) have shown that compared with the LAPW method, the APW+lo scheme converges at a much lower cost to essentially the same results. [32]

2.4 Wannier functions

In this section, the Wannier representation is presented in the context of the Wien2Wannier software [4] and the MC program.

For the independent-particle approximation in a perfect crystal, electron states are conventionally described by Bloch waves labelled by a band index n and a wave vector $\boldsymbol{k}$. An alternate representation in real space was introduced by Gregory Wannier in 1937. This localized orbital in a periodic structure description is now known as a Wannier representation. In the Wannier representation each state is labelled by band index n and lattice vector $\boldsymbol{R}$, making it a real-space representation of the electron states.

Wannier transformation

According to Bloch's theorem a common eigenstate of the one-electron Hamiltonian $\hat{\mathcal{H}}$ and the lattice-translation operator $\hat{\mathcal{T}}_{\mathcal{R}}$ is given by:

$$\psi_{n\boldsymbol{k}}(\boldsymbol{r}) = e^{i\phi_n(\boldsymbol{r})} u_{n\boldsymbol{k}}(\boldsymbol{r}) e^{i\boldsymbol{k}\cdot\boldsymbol{r}} \tag{2.31}$$

One demands that $u_{n\boldsymbol{k}}(\boldsymbol{r})$ has the periodicity of the lattice and $e^{i\phi_n(\boldsymbol{r})}$ the periodicity of the corresponding reciprocal lattice. The latter, typically not written out explicitly, has been written out here to emphasise that is not assigned by Schroedinger's equation and therefore offers an arbitrary phase to the Bloch wavefunction. This phase hence makes a Bloch-state non-unique. As stated earlier, a real-space representation is more convenient in many applications, for instance when dealing with transport properties [8]. One finds such a representation by a Fourier transformation of the Bloch state into a Wannier state. This indeterminacy of the Bloch state represented by $e^{i\phi_n(\boldsymbol{r})}$ does indeed propagate to the Wannier representation which also becomes non-unique. A Wannier representation of the Bloch state is given as:

$$\omega_n(\boldsymbol{r} - \boldsymbol{R}) = |\boldsymbol{R}n\rangle = \frac{V}{\left(2\pi\right)^3} \int_{BZ} \sum_{m=1}^{N} U_{mn}^{(\boldsymbol{k})} |\psi_{m\boldsymbol{k}}\rangle \, e^{-i\boldsymbol{k}\cdot\boldsymbol{R}} d\boldsymbol{k} \tag{2.32}$$

where the label $\boldsymbol{R}$ denotes a lattice point and n energy band. V represents the crystal volume and $\varphi_n(\boldsymbol{k}+\boldsymbol{G}) = \varphi(\boldsymbol{k})$ for G denoting any reciprocal lattice vector. The phase factor $U_{mn}^{(\boldsymbol{k})}$ represents the arbitrariness inherited from the Bloch-function phase factor $e^{i\phi_n(\boldsymbol{r})}$ resulting in the indeterminacy of the Wannier representation. The set $\{|\boldsymbol{R}n\rangle\}$ constitute an orthonormal basis [8] and $|\boldsymbol{R}n\rangle$ is transformed into $|\boldsymbol{R'}n\rangle$ by a translation of the lattice

vector $\boldsymbol{R'} - \boldsymbol{R}$.

Finally, the inverse transformation, carrying one from the Wannier representation to Bloch, is given by

$$\psi_{n\boldsymbol{k}}(\boldsymbol{r}) = \sum_{\boldsymbol{R}} e^{i\boldsymbol{k}\cdot\boldsymbol{r}} \left|\boldsymbol{R}n\right\rangle \tag{2.33}$$

2.4.1 Maximally localized Wannier functions

The gauge freedom present in the Bloch state and inherited by the Wannier representation may be used to maximally localize the Wannier functions. This localization corresponds to choosing a particular unitary matrix $U_{mn}^{(\boldsymbol{k})}$ in (2.32). In order to carry out this procedure, one first introduces a well-defined localization-criterion

$$\Omega = \sum_{n} \left[\left\langle \boldsymbol{0}n\right| \boldsymbol{r}^2 \left|\boldsymbol{0}n\right\rangle - \left\langle \boldsymbol{0}n\right| \boldsymbol{r} \left|\boldsymbol{0}n\right\rangle^2 \right] \tag{2.34}$$

where Ω denotes the spread in the Wannier function and $\boldsymbol{r}$ is the position operator. The sum runs over all basis functions. Details around the procedure of minimizing the spread (2.34) are given by Marzari et al. (2012) [8], but one thing is worth pointing out: in 1962 Blount showed the matrix elements in Ω may be expressed in terms of Bloch orbitals, ∇_k and ∇_k^2 [33]

$$\left\langle \boldsymbol{R}n\right| \boldsymbol{r} \left|\boldsymbol{0}m\right\rangle = i\frac{V}{\left(2\pi\right)^3} \int d\boldsymbol{k} e^{i\boldsymbol{k}\cdot\boldsymbol{R}} \left\langle u_{n\boldsymbol{k}}\right| \nabla_{\boldsymbol{k}} \left|u_{m\boldsymbol{k}}\right\rangle \tag{2.35}$$

$$\left\langle \boldsymbol{R}n\right| \boldsymbol{r}^2 \left|\boldsymbol{0}m\right\rangle = -\frac{V}{\left(2\pi\right)^3} \int d\boldsymbol{k} e^{i\boldsymbol{k}\cdot\boldsymbol{R}} \left\langle u_{n\boldsymbol{k}}\right| \nabla_{\boldsymbol{k}}^2 \left|u_{m\boldsymbol{k}}\right\rangle \tag{2.36}$$

To evaluate the matrix elements of (2.35) and (2.36), the Bloch orbitals are assumed to be discretized onto a uniform mesh (a uniform Monkhorst-Pack mesh [34]). Using finite-differences to evaluate the matrix elements of ∇_k and ∇_k^2, Marzari et al (2012) show that the information needed is the overlap between Bloch orbitals at neighbouring $\boldsymbol{k}$ points

$$G_{nm}(\boldsymbol{k}, \boldsymbol{b}) = \langle u_{m,\boldsymbol{k}} | u_{n,\boldsymbol{k}+\boldsymbol{b}} \rangle \tag{2.37}$$

If the overlaps (2.37) are tabulated, the localization, and equally important the effect any unitary transformation may have on the localization, is available through (2.34), (2.35) and (2.36) without the need to recalculate overlaps or through any other interaction with the original Bloch states used to generate Wannier functions. Furthermore, looking back at the calculation of scattering rates with eigenfunctions in (2.1) and (2.3), it becomes clear that the information needed to construct MLWFs may be used to calculate scattering rates with the LAPW basis. The overlaps (2.37) are in fact tabulated in the program Wien2Wannier to provide the necessary input for the program Wannier90 which constructs the MLWFs, and could potentially be extracted to calculate scattering rates as described in Chapter 2.1. This is the computationally cost-efficient way of acquiring scattering rates since the overlaps are given free of any computational costs. But the overlaps needed in the construction of

MLWF's are only between neighbouring points in the Brillouin-zone. The initial and final charge carrier states can generally not be restricted to neighbouring Brillouin zone points. Since the initial and final eigenfunctions may not even be restricted to the first Brillouin zone, the overlaps needed to calculate scattering rates represents only a fraction of the overlaps needed for determining individual scattering rates. We therefore conclude that although overlaps between LAPW basis functions are used to construct MLWFs, these are not relevant enough for the calculation of scattering rates to be reused.

Chapter 3

Scattering rates in LAPW and Wannier basis

In this section, an expression for the overlap (2.2) between initial and final electron states for a scattering event is derived in the LAPW method and Wannier representation. The objective is to obtain expressions for the overlap that are suitable for numerical integration over the first Brillouin zone. These may then be used to calculate the scattering rates for a particular scattering mechanism as described in Chapter 2.1.

The general overlap that is needed takes spin-flipping into account and reads

$$G_{nn'}(\boldsymbol{k},\boldsymbol{k'}) = \frac{1}{2}\sum_{\sigma}\sum_{\sigma'}\Big|\int_{\text{u.c}} d^3r u^*_{n'\boldsymbol{k'}\sigma'} u_{n\boldsymbol{k}\sigma} e^{i\boldsymbol{K}\cdot\boldsymbol{r}}\Big|^2 \tag{3.1}$$

We will only derive expressions for

$$G_{n\boldsymbol{\sigma},n'\sigma'}(\boldsymbol{k},\boldsymbol{k'}) = \Big|\int_{\text{u.c}} d^3r u^*_{n'\boldsymbol{k'}\sigma'} u_{n\boldsymbol{k}\sigma} e^{i\boldsymbol{K}\cdot\boldsymbol{r}}\Big|^2 \tag{3.2}$$

since the generalization is straightforward once these are given. For tidier notation, spin indices are henceforth omitted

$$G'_{nn'}(\boldsymbol{k},\boldsymbol{k'}) = \Big|\int_{\text{u.c}} d^3r u^*_{n'\boldsymbol{k'}} u_{n\boldsymbol{k}} e^{i\boldsymbol{K}\cdot\boldsymbol{r}}\Big|^2 \tag{3.3}$$

3.1 LAPW overlap

We start by writing out the absolute square of (3.3)

$$G'_{nn'}(\boldsymbol{k},\boldsymbol{k'}) = \int_{\text{u.c}} d^3r u^*_{n'\boldsymbol{k'}}(\boldsymbol{r}) u_{n\boldsymbol{k}}(\boldsymbol{r}) e^{i\boldsymbol{K}\cdot\boldsymbol{r}} \int_{\text{u.c}} d^3r' u_{n'\boldsymbol{k'}}(\boldsymbol{r'}) u^*_{n\boldsymbol{k}}(\boldsymbol{r'}) e^{-i\boldsymbol{K}\cdot\boldsymbol{r'}} \tag{3.4}$$

where in the above, the first integral is the complex conjugate of the second. We will derive an expression for the first integral, and once known it is simply multiplied with its complex-conjugate to yield the LHS of (3.4). As a reminder the LAPW basis reads

$$u_{\boldsymbol{k}}(\boldsymbol{r}) = \begin{cases} \sum_{lm}\left[a_{\boldsymbol{k},lm}u_{1,l}(r,E_l) + b_{\boldsymbol{k},lm}\dot{u}_{1,l}(r,E_l) + c_{\boldsymbol{k},lm}u_{2,l}(r_)\right]Y_{lm}(\boldsymbol{r},E_l) & \text{region I} \\ \frac{1}{\sqrt{V}}\sum_{\boldsymbol{G}} C_{\boldsymbol{k}}(\boldsymbol{G}) e^{i(\boldsymbol{k}+\boldsymbol{G})\cdot\boldsymbol{r}} & \text{region II} \end{cases} \tag{3.5}$$

where compared with the expression (2.23) given in chapter 2, indices for the particular sphere β in region I and spin σ are implied. Band index is also omitted even though the expansion coefficients depend on it.

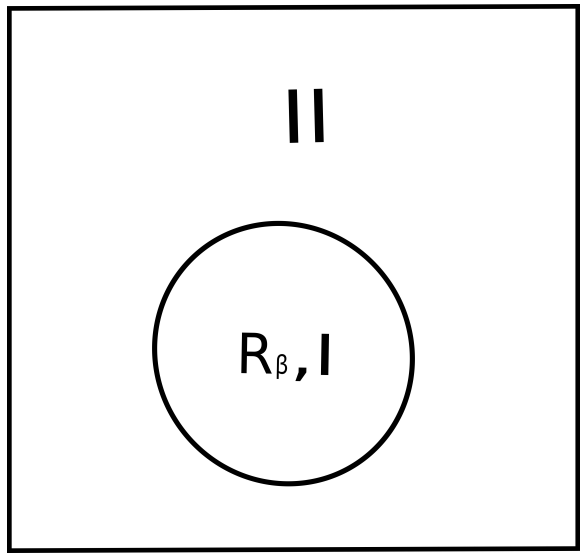

Figure 3.1: *Partitioning of the unit cell into two regions: atomic spheres centered around $\boldsymbol{R}_\beta$ in region I and an interstital part, region II. There may generally be more than one sphere making up region I, each sphere corresponding to a nucleus in the unit cell.*

3.1.1 Region I

In order to evaluate the overlap in region I, we first focus our attention on a given sphere β. The plane-wave $e^{i\boldsymbol{K}\cdot\boldsymbol{r}}$, appearing in (3.3) is expanded into Bessel functions and Spherical harmonics with their origin at point $\boldsymbol{R_\beta}$ at the center of sphere β in region I (see figure 3.1).

$$e^{i\boldsymbol{K}\cdot\boldsymbol{r}} = 4\pi e^{i\boldsymbol{K}\cdot\boldsymbol{R_\beta}} \sum_l i^l j_l(br_\beta) \sum_m Y_{lm}(\hat{\boldsymbol{K}}) Y_{lm}(\hat{\boldsymbol{r}}_{\boldsymbol{\beta}}) \tag{3.6}$$

where $j_l(|\boldsymbol{K}|r_\beta)$ is a Bessel function, Y_{lm} is a Spherical Harmonics function and finally $\hat{\boldsymbol{K}}$ and $\hat{\boldsymbol{r}}_{\boldsymbol{\beta}}$ unit vectors pointing in the same direction as $\boldsymbol{K}$ and $\boldsymbol{r}_\beta$, respectively. 'i' denotes the imaginary unit. While the initial plane-wave was expressed in terms of a global origin, we have now managed to change to $\boldsymbol{r}_\beta$ which is centered around the sphere β, making the overlap in region I tractable.

Inserting the basis expression for region I, from equation (3.5), and the Bessel expansion (3.6) into the first overlap integral of (3.4), $\int_{\text{u.c}} d^3r u^*_{n'\boldsymbol{k'}}(\boldsymbol{r}) u_{n\boldsymbol{k}}(\boldsymbol{r}) e^{i\boldsymbol{K}\cdot\boldsymbol{r}}$, we get an expression for the overlap in region I

$$\begin{aligned}
&\sum_{l_1m_1}\sum_{l_2m_2}\sum_{l_3m_3}\int_{\text{u.c}} \\
&\big[a^*_{\boldsymbol{k'},l_1m_1} u^*_{1,l_1}(r_\beta) + b^*_{\boldsymbol{k'},l_1m_1}\dot{u}^*_{1,l_1}(r_\beta) + c^*_{\boldsymbol{k'},l_1m_1} u^*_{2,l_1}(r_\beta)\big] Y^*_{l_1m_1}(\boldsymbol{r_\beta})\times \\
&4\pi e^{i\boldsymbol{K}\cdot\boldsymbol{R_\beta}} i^{l_2} j_{l_2}(br_\beta) Y_{l_2m_2}(\hat{\boldsymbol{K}}) Y_{l_2m_2}(\hat{\boldsymbol{r}}_{\boldsymbol{\beta}})\times \\
&\big[a_{\boldsymbol{k},l_3m_3} u_{1,l_3}(r_\beta) + b_{\boldsymbol{k},l_3m_3}\dot{u}_{1,l_3}(r_\beta) + c_{\boldsymbol{k},l_3m_3} u_{2,l_3}(r_\beta)\big] Y_{l_3m_3}(\boldsymbol{r_\beta})
\end{aligned} \tag{3.7}$$

where the first line is inserted for $u^*_{n'\boldsymbol{k'}}(\boldsymbol{r})$, second line is inserted for the expansion of $e^{i\boldsymbol{K}\cdot\boldsymbol{r}}$ and the third line is inserted for $u_{n\boldsymbol{k}}(\boldsymbol{r})$. Since these depend on their own respective summation indices l and m, a sub-subindex has been added to prevent mixing them up: 1 corresponds to expansion coefficients for $u^*_{n'\boldsymbol{k'}}(\boldsymbol{r})$, 2 corresponds to expansion coefficients for $e^{i\boldsymbol{K}\cdot\boldsymbol{r}}$ and finally 3 corresponds to $u_{n\boldsymbol{k}}(\boldsymbol{r})$. (3.7) consists of radial and an angular integrals over the chosen sphere β in region I . Sorting the different factors out, we are left with a prefactor given by

$$4\pi e^{i\boldsymbol{K}\cdot\boldsymbol{R_\beta}} i^{l_2} Y_{l_2m_2}(\hat{\boldsymbol{K}}) \tag{3.8}$$

the angular integral is given by

$$\int_{\phi=0}^{2\pi}\int_{\theta=0}^{\pi} d\Omega Y^*_{l_1m_1}(\hat{\boldsymbol{r}}_\beta) Y_{l_2m_2}(\hat{\boldsymbol{r}}_\beta) Y_{l_3m_3}(\hat{\boldsymbol{r}}_\beta) \tag{3.9}$$

and the radial integral by

$$\begin{aligned}
&\int_0^{\rho_\beta} dr_\beta r_\beta^2 \big[a^*_{\boldsymbol{k'},l_1m_1} u^*_{1,l_1}(r_\beta) + b^*_{\boldsymbol{k'},l_1m_1}\dot{u}^*_{1,l_1}(r_\beta) + c^*_{\boldsymbol{k'},l_1m_1} u^*_{2,l_1}(r_\beta)\big] j_{l_2}(|\boldsymbol{K}|r_\beta) \\
&\big[a_{\boldsymbol{k},l_3m_3} u_{1,l_3}(r_\beta) + b_{\boldsymbol{k},l_3m_3}\dot{u}_{1,l_3}(r_\beta) + c_{\boldsymbol{k},l_3m_3} u_{2,l_3}(r_\beta)\big]
\end{aligned} \tag{3.10}$$

where the radial integral goes from radius zero to ρ_β, the radius of atomic sphere β. The contribution to equation (3.4) now reads

$$\begin{aligned}
&\sum_{l_1 m_1} \sum_{l_2 m_2} \sum_{l_3 m_3} \\
&4\pi e^{i\boldsymbol{K}\cdot\boldsymbol{R_\beta}} i^{l_2} Y_{l_2 m_2}(\hat{\boldsymbol{K}}) \\
&\int_{\phi=0}^{2\pi} \int_{\theta=0}^{\pi} d\Omega Y^*_{l_1 m_1}(\hat{\boldsymbol{r}}_\beta) Y_{l_2 m_2}(\hat{\boldsymbol{r}}_\beta) Y_{l_3 m_3}(\hat{\boldsymbol{r}}_\beta) \\
&\int_0^{\rho_\beta} dr_\beta r_\beta^2 \big[a^*_{\boldsymbol{k'},l_1 m_1} u^*_{1,l_1}(r_\beta) + b^*_{\boldsymbol{k'},l_1 m_1} \dot{u}^*_{1,l_1}(r_\beta) + c^*_{\boldsymbol{k'},l_1 m_1} u^*_{2,l_1}(r_\beta)\big] j_{l_2}(|\boldsymbol{K}| r_\beta) \\
&\big[a_{\boldsymbol{k},l_3 m_3} u_{1,l_3}(r_\beta) + b_{\boldsymbol{k},l_3 m_3} \dot{u}_{1,l_3}(r_\beta) + c_{\boldsymbol{k},l_3 m_3} u_{2,l_3}(r_\beta)\big]
\end{aligned} \tag{3.11}$$

But this is only the contribution from region I. We also need the contribution from region II.

3.1.2 Region II

We similarly evaluate the overlap for region II by inserting the plane-wave basis in equation (3.5) into the first integral on the RHS in (3.4)

$$\frac{1}{V} \sum_{\boldsymbol{G_1 G_2}} C^*_{\boldsymbol{k'}}(\boldsymbol{G_1}) C_{\boldsymbol{k}}(\boldsymbol{G_2}) \int_{II} d^3 r e^{i(\boldsymbol{K})\cdot\boldsymbol{r}} e^{i(\boldsymbol{k'}+\boldsymbol{G_2})\cdot\boldsymbol{r}} e^{-i(\boldsymbol{G_1}+\boldsymbol{k})\cdot\boldsymbol{r}} \tag{3.12}$$

We assume now that $e^{i(\boldsymbol{k'}-\boldsymbol{k})\cdot\boldsymbol{r}} \approx 1$ which should work if the unit cell is sufficiently small

$$\frac{1}{V} \sum_{\boldsymbol{G_1 G_2}} C^*_{\boldsymbol{k'}}(\boldsymbol{G_1}) C_{\boldsymbol{k}}(\boldsymbol{G_2}) \int_{II} d^3 r e^{i(\boldsymbol{G_2}-\boldsymbol{G_1}+\boldsymbol{K})\cdot\boldsymbol{r}} \tag{3.13}$$

where the integral runs over region II. We now split the integral $\int_{II} d^3\boldsymbol{r} e^{i(\boldsymbol{K}-\boldsymbol{K'})\cdot\boldsymbol{r}}$ into one over the unit cell and another over region I, the latter subtracted to give the right integration domain

$$\begin{aligned}
&\frac{1}{V} \sum_{\boldsymbol{G_1 G_2}} C^*_{\boldsymbol{k'}}(\boldsymbol{G_1}) C_{\boldsymbol{k}}(\boldsymbol{G_2}) \int_{u.c} d^3 r e^{i(\boldsymbol{G_2}-\boldsymbol{G_1}+\boldsymbol{K})\cdot\boldsymbol{r}} - \\
&\frac{1}{V} \sum_{\boldsymbol{G_1 G_2}} C^*_{\boldsymbol{k'}}(\boldsymbol{G_1}) C_{\boldsymbol{k}}(\boldsymbol{G_2}) \int_{I} d^3 r e^{i(\boldsymbol{G_2}-\boldsymbol{G_1}+\boldsymbol{K})\cdot\boldsymbol{r}}
\end{aligned} \tag{3.14}$$

Since $\boldsymbol{G_1}$, $\boldsymbol{G_2}$ and $\boldsymbol{K}$ are recirpocal lattice vectors, so is $\boldsymbol{G_2} - \boldsymbol{G_1} + \boldsymbol{K}$. This results in a delta-function for the integral over the unit cell

$$\frac{1}{V} \sum_{\boldsymbol{G_1 G_2}} \big(V\delta(\boldsymbol{G_2} - \boldsymbol{G_1} + \boldsymbol{K})\big) \tag{3.15}$$

The integral over region I is on the other hand a sum over each and every atomic sphere, denoted by β in the unit cell. $\boldsymbol{r}$ represents the coordinate within the unit cell, so we write $\boldsymbol{r} = \boldsymbol{R_\beta} + \boldsymbol{r_\beta}$ to express the integral in terms of coordinates centered inside each sphere β of region I

$$\frac{1}{V}\sum_{\boldsymbol{G_1 G_2}}\sum_{\beta} C^*_{\boldsymbol{k'}}(\boldsymbol{G_1})C_{\boldsymbol{k}}(\boldsymbol{G_2})e^{i(\boldsymbol{G_2}-\boldsymbol{G_1}+\boldsymbol{K})\cdot\boldsymbol{R_\beta}}\int_I d^3r_\beta e^{i(\boldsymbol{G_2}-\boldsymbol{G_1}+\boldsymbol{K})\cdot\boldsymbol{r_\beta}} \tag{3.16}$$

and the sum runs over all atomic spheres β. Orienting the z-axis along $|\boldsymbol{G_2} - \boldsymbol{G_1} + \boldsymbol{K}|$ and switching to spherical coordinates, the integral may be evaluated to yield

$$\frac{1}{V}\sum_{\boldsymbol{G_1 G_2}}\sum_{\beta} 3V_\beta e^{i(\boldsymbol{G_2}-\boldsymbol{G_1}+\boldsymbol{K})\cdot\boldsymbol{R_\beta}}\frac{sin(x) - xcos(x)}{x^3} \tag{3.17}$$

where $x = \rho_\beta|\boldsymbol{G_2} - \boldsymbol{G_1} + \boldsymbol{K}|$, $V_\beta = \frac{4}{3}\pi\rho_\beta^3$ and ρ_β is radius of sphere β. By adding the contributions to the overlap from region I and II, i.e (3.11) and (3.17), we obtain the first integral in (3.4). The second integral is simply the complex-conjugated of the first, and thus we have the overlap.

The expression presented here is based on an expression implemented in Wien2Wannier.[4] As mentioned in the end of Chapter 2.4, the computed overlaps in Wien2Wannier are restricted to neighbouring overlaps and were not found to be useful. The numerical expression they present is nonetheless suitable in our case since the overlap considered is otherwise the same apart from some slight modifications arising from the overlap we are interested in. As seen from equation (3.1), our overlap has an exponential factor $e^{i\boldsymbol{K}\cdot\boldsymbol{r}}$, and we also average over initial spin-states and sum over final ones.

3.1.3 Total overlap

To summarize, we have an expression from region I

$$\begin{aligned}
&\sum_{l_1m_1}\sum_{l_2m_2}\sum_{l_3m_3}\\
&4\pi e^{i\boldsymbol{K}\cdot\boldsymbol{R_\beta}} i^{l_2} Y_{l_2m_2}(\hat{\boldsymbol{K}})\\
&\int_{\phi=0}^{2\pi}\int_{\theta=0}^{\pi} d\Omega Y^*_{l_1m_1}(\hat{\boldsymbol{r}}_\beta)Y_{l_2m_2}(\hat{\boldsymbol{r}}_\beta)Y_{l_3m_3}(\hat{\boldsymbol{r}}_\beta)\\
&\int_0^{\rho_\beta} dr_\beta r_\beta^2\big[a^*_{\boldsymbol{k'},l_1m_1}u^*_{1,l_1}(r_\beta) + b^*_{\boldsymbol{k'},l_1m_1}\dot{u}^*_{1,l_1}(r_\beta) + c^*_{\boldsymbol{k'},l_1m_1}u^*_{2,l_1}(r_\beta)\big]j_{l_2}(|\boldsymbol{K}|r_\beta)\\
&\big[a_{\boldsymbol{k},l_3m_3}u_{1,l_3}(r_\beta) + b_{\boldsymbol{k},l_3m_3}\dot{u}_{1,l_3}(r_\beta) + c_{\boldsymbol{k},l_3m_3}u_{2,l_3}(r_\beta)\big]
\end{aligned} \tag{3.18}$$

and the expression from region II reads

$$\frac{1}{V}\sum_{\boldsymbol{G_1 G_2}} V\delta(\boldsymbol{G_2} - \boldsymbol{G_1} + \boldsymbol{K}) - \sum_{\beta} 3V_\beta e^{i(\boldsymbol{G_2}-\boldsymbol{G_1}+\boldsymbol{K})\cdot\boldsymbol{R_\beta}}\frac{sin(x) - xcos(x)}{x^3} \tag{3.19}$$

Added together, these correspond to the overlap integral

$$\int_{\text{u.c}} d^3r u^*_{n'\boldsymbol{k'}}(\boldsymbol{r}) u_{n\boldsymbol{k}}(\boldsymbol{r}) e^{i\boldsymbol{K}\cdot\boldsymbol{r}} \tag{3.20}$$

and finally, when multiplied with its complex conjugated, we have the desired overlap expression

$$\begin{aligned} G'_{nn'}(\boldsymbol{k},\boldsymbol{k'}) = \int_{\text{u.c}} d^3r u^*_{n'\boldsymbol{k'}}(\boldsymbol{r}) u_{n\boldsymbol{k}}(\boldsymbol{r}) e^{i\boldsymbol{K}\cdot\boldsymbol{r}} \\ \int_{\text{u.c}} d^3r' u_{n'\boldsymbol{k'}}(\boldsymbol{r'}) u^*_{n\boldsymbol{k}}(\boldsymbol{r'}) e^{-i\boldsymbol{K}\cdot\boldsymbol{r'}} \end{aligned} \tag{3.21}$$

3.2 Wannier overlap

Starting with the overlap factor between two Bloch states, we use the inverse Wannier transformation (2.33) to acquire the overlap factor in terms of Wannier overlaps. The overlap factor is given by

$$G_{nn'}(\boldsymbol{k},\boldsymbol{k'}) = \Big| \int_{\text{u.c}} d^3r u^*_{n'\boldsymbol{k'}} u_{n\boldsymbol{k}} e^{i\boldsymbol{K}\cdot\boldsymbol{r}} \Big|^2 \tag{3.22}$$

where $\boldsymbol{K} = \boldsymbol{k} - \boldsymbol{k'} + \boldsymbol{q}$ is the reciprocal lattice vector, $u_{n\boldsymbol{k}}$ is the cell-periodic part of the Bloch state and the integral runs over the unit cell. $\boldsymbol{k}$ and $\boldsymbol{k'}$ are initial and final scattering wavevectors respectively, and $\boldsymbol{q}$ is a Fourier component of the perturbed potential causing scattering. Since the inverse Wannier transform (2.33) in its current form is related to the general Bloch state, we express it in terms of the cell-periodic part in order to insert the inverse Wannier transform into (3.22). The cell-periodic part $u_{n\boldsymbol{k}}$ of the Bloch state is associated with the BlocH state through

$$\psi_{n\boldsymbol{k}}(\boldsymbol{r}) = u_{n\boldsymbol{k}}(\boldsymbol{r}) e^{i\boldsymbol{k}\cdot\boldsymbol{r}} \tag{3.23}$$

The inverse Wannier transformation in terms of the cell-periodic part of the wavefunction now reads

$$\psi_{n\boldsymbol{k}}(\boldsymbol{r}) = \sum_{\boldsymbol{R}} e^{i\boldsymbol{k}\cdot\boldsymbol{R}} \omega_{n\boldsymbol{R}}(\boldsymbol{r}) \tag{3.24}$$

Isolating the Bloch periodic part of the wavefunction on LHS yields

$$u_{n\boldsymbol{k}}(\boldsymbol{r}) = e^{-i\boldsymbol{k}\cdot\boldsymbol{r}} \sum_{\boldsymbol{R}} e^{i\boldsymbol{k}\cdot\boldsymbol{R}} \omega_{n\boldsymbol{R}}(\boldsymbol{r}) \tag{3.25}$$

We will also need the complex-conjugated Bloch periodic function

$$u^*_{n\boldsymbol{k}}(\boldsymbol{r}) = e^{i\boldsymbol{k}\cdot\boldsymbol{r}} \sum_{\boldsymbol{R}} e^{-i\boldsymbol{k}\cdot\boldsymbol{R}} \omega^*_{n\boldsymbol{R}}(\boldsymbol{r}) \tag{3.26}$$

Inserting the Bloch periodic functions (3.25) and (3.26) into (3.22) yields

$$G_{nn'}(\boldsymbol{k},\boldsymbol{k'}) = \\ \Big| \int_{\text{u.c}} d^3r e^{i\boldsymbol{k'}\cdot\boldsymbol{r}} \sum_{\boldsymbol{R'}} e^{-i\boldsymbol{k'}\cdot\boldsymbol{R'}} \omega^*_{n'\boldsymbol{R'}}(\boldsymbol{r}) e^{-i\boldsymbol{k}\cdot\boldsymbol{r}} \sum_{\boldsymbol{R''}} e^{i\boldsymbol{k}\cdot\boldsymbol{R''}} \omega_{n\boldsymbol{R''}}(\boldsymbol{r}) e^{i\boldsymbol{K}\cdot\boldsymbol{r}} \Big|^2 \tag{3.27}$$

Reorganizing a bit

$$G_{nn'}(\boldsymbol{k},\boldsymbol{k'}) = \Big| \sum_{\boldsymbol{R'}} \sum_{\boldsymbol{R}} e^{-i\boldsymbol{k'}\cdot\boldsymbol{R'}+i\boldsymbol{k}\cdot\boldsymbol{R}} \int_{\text{u.c}} d^3r e^{i(\boldsymbol{K}+\boldsymbol{k'}-\boldsymbol{k})\cdot\boldsymbol{r}} \omega^*_{n'\boldsymbol{R'}}(\boldsymbol{r}) \omega_{n\boldsymbol{R}}(\boldsymbol{r}) \Big|^2 \tag{3.28}$$

But since $\boldsymbol{K}+\boldsymbol{k'}-\boldsymbol{k}=\boldsymbol{q}$, we get

$$G_{nn'}(\boldsymbol{k},\boldsymbol{k'}) = \Big| \sum_{\boldsymbol{R'}} \sum_{\boldsymbol{R}} e^{-i\boldsymbol{k'}\cdot\boldsymbol{R'}+i\boldsymbol{k}\cdot\boldsymbol{R}} \int_{\text{u.c}} d^3r e^{i\boldsymbol{q}\cdot\boldsymbol{r}} \omega^*_{n'\boldsymbol{R'}}(\boldsymbol{r}) \omega_{n\boldsymbol{R}}(\boldsymbol{r}) \Big|^2 \tag{3.29}$$

Writing out the absolute square

$$\begin{aligned} &G_{nn'}(\boldsymbol{k},\boldsymbol{k'}) = \\ &\sum_{\boldsymbol{R'_1}} \sum_{\boldsymbol{R_1}} e^{-i\boldsymbol{k'}\cdot\boldsymbol{R'_1}+i\boldsymbol{k}\cdot\boldsymbol{R_1}} \int_{\text{u.c}} d^3r e^{i\boldsymbol{q}\cdot\boldsymbol{r}} \omega^*_{n'\boldsymbol{R'_1}}(\boldsymbol{r}) \omega_{n\boldsymbol{R_1}}(\boldsymbol{r}) \Big] \times \\ &\Big[\sum_{\boldsymbol{R'_2}} \sum_{\boldsymbol{R_2}} e^{i\boldsymbol{k'}\cdot\boldsymbol{R'_2}-i\boldsymbol{k}\cdot\boldsymbol{R_2}} \int_{\text{u.c}} d^3r' e^{-i\boldsymbol{q}\cdot\boldsymbol{r'}} \omega_{n'\boldsymbol{R'_2}}(\boldsymbol{r'}) \omega^*_{n\boldsymbol{R_2}}(\boldsymbol{r'}) \Big] \end{aligned} \tag{3.30}$$

and reorganizing a bit

$$\begin{aligned} &G_{nn'}(\boldsymbol{k},\boldsymbol{k'}) = \\ &\sum_{\boldsymbol{R'_1}} \sum_{\boldsymbol{R_1}} \sum_{\boldsymbol{R'_2}} \sum_{\boldsymbol{R_2}} e^{i\boldsymbol{k'}\cdot(\boldsymbol{R'_2}-\boldsymbol{R'_1})-i\boldsymbol{k}\cdot(\boldsymbol{R_2}-\boldsymbol{R_1})} \\ &\int_{\text{u.c}} d^3r e^{i\boldsymbol{q}\cdot\boldsymbol{r}} \omega^*_{n'\boldsymbol{R'_1}}(\boldsymbol{r}) \omega_{n\boldsymbol{R_1}}(\boldsymbol{r}) \int_{\text{u.c}} d^3r' e^{-i\boldsymbol{q}\cdot\boldsymbol{r'}} \omega_{n'\boldsymbol{R'_2}}(\boldsymbol{r'}) \omega^*_{n\boldsymbol{R_2}}(\boldsymbol{r'}) \end{aligned} \tag{3.31}$$

What we are left with is a sum over four summation variables, each one running over all lattice points $\boldsymbol{R}$ in the electronic structure. For each term in the summation, two integrals involving Wannier functions and an interaction is involved. Therefore, at the current stage, the expression (3.31) for $G_{nn'}(\boldsymbol{k},\boldsymbol{k'})$ is not tractable for the Monte Carlo program. In order for that to happen, the summation should ideally be limited by a cut-off radius to limit the computational costs involved. In addition, a scheme should be developed to numerically evaluate the overlaps of Wannier functions in each term.

Chapter 4

Results and discussion

In this section, results for materials GaAs, Si and HgCdTe are presented. For Silicon and GaAs, the effect of spin-orbit coupling on the valence band is investigated, and symmetries of the band edge wavefunctions presented. Silicon and GaAs are well-studied semiconductor materials and therefore offer an opportunity to test Wien2k, Wien2Wannier and Wannier90 on these materials. The properties of Silicon and GaAs tested against may for example be found in J. Singh, *Electronic and optoelectronic properties of semiconductor structures* and Ridley B. K, *Quantum Processes in Semiconductors* [2] [14]. For CMT, the badgap and the effect of LDA+U is discussed.

Bandstructure plots for every material are plotted in the same format, i.e along the same symmetry lines. These are from left to right on the plots (in reciprocal lattice vector units)

$$\begin{aligned} L &= (\frac{1}{2}, 0, 0) \\ \Gamma &= (0, 0, 0) \\ X &= (0, \frac{1}{2}, \frac{1}{2}) \\ K.4 &= (0, \frac{5}{8}, \frac{3}{8}) \\ \Gamma &= (0, 0, 0) \end{aligned} \tag{4.1}$$

4.1 GaAs

Gallium arsenide is a III-V direct bandgap semiconductor with a zinc blende structure. Since GaAs is often presented in elementary textbooks on semiconductors, it provides a good opportunity to test the validity of the input data acquired from Wien2k and Wannier90 which will be used for the Monte Carlo transport program. The lattice parameter used is $a = 5.65$ Å, acquired from *crystallography.net*. The effect of spin-orbit coupling

on the degeneracy in valence band is investigated, and symmetries of the band edge states presented.

It is well-known that essentially all semiconductors have a four-fold symmetry at the top most valence band, and a 2-fold symmetry band slightly below. However, a tight-binding calculation using s and p orbitals , where relativistic effects are not taken into account, will incorrectly yield a six-fold symmetry at the valence band edge. Thus, a first-principles calculations made on GaAs excluding spin-orbit effects can be expected to yield a six-fold symmetry at the valence band edge. The bandstructure for GaAs without spin-orbit effects, calculated with Wien2k, is shown in figure 4.1a. This matches well with calculations made on GaAs with DFT where spin-orbit effects have been excluded. The valence bands that give this six-fold symmetry are highlighted in blue and red, obtaining their peak at γ just under the shaded area across the figure representing the band gap. The six-fold symmetry corresponds to the three orbitals px, py and pz, each state associated with a spin-up state and a spin-down state.

Taking spin-orbit effects into account, we expect this degeneracy to be lifted and the symmetry of band edge states to match those of experiments on semiconductors. In other words, there should be a 4-fold symmetry at the top most valence band, and a 2-fold symmetry band slightly below. Results are shown in figure 4.1b. As indicated, the degeneracy of the valence band has been lifted around the band edge to form bands conventionally named (I) the Heavy Hole (in blue), (II) the Light Hole (in red) and (III) the Split-Off band. Exactly at the valence band edge, there is a two-fold symmetry due to the Heavy-Hole - Light-Hole degeneracy, and the Split-Off band falls below the Heavy-Hole - Ligh-Hole band edge. Taking spin degeneracy into account, one arrives at the experimentally correct band edge symmetry of four-fold symmetry at the top valence band with another two-fold symmetry slightly below.

Another interesting feature of GaAs is its direct bandgap. Direct bandgap semiconductors are characterized by the lowest point on the conduction band occurring at Γ. The electron states near the conduction band have a central cell periodic state that is spherically symmetric, i.e we say the states are described by s-orbitals (as one moves away from the conduction band edge however, p-orbitals mix in). The valence band edge is analogously made up of p-orbitals with a spherically symmetric state further below these states. The symmetries exhibited by the central cell part of the valence band are however similar. Using Wien2Wannier and Wannier90 to post-process the eigenfunctions acquired from Wien2k, we arrive at Wannier functions for states near the band edge that are plotted using XCrysDen [ref]. This has been done for the non-spin-orbit case of GaAs. Isosurfaces, i.e points of equal absolute value of the Wannier functions are plotted in the conventional cell of GaAs, with a purple bullet indicating a gallium-atom, and yellow bullet indicating an arsenide-atom. Red and blue surfaces indicate same absolute value but different sign of the isosurface plotted. Figure 4.2a shows an isosurface of the valence band state corresponding to the bottom valence band (black) depicted in figure 4.1a. As can be seen from the plot, the isosurface is spherically symmetric and centered around a gallium atom. In figure 4.2b, the valence band edge states are plotted. These are also centered around a gallium

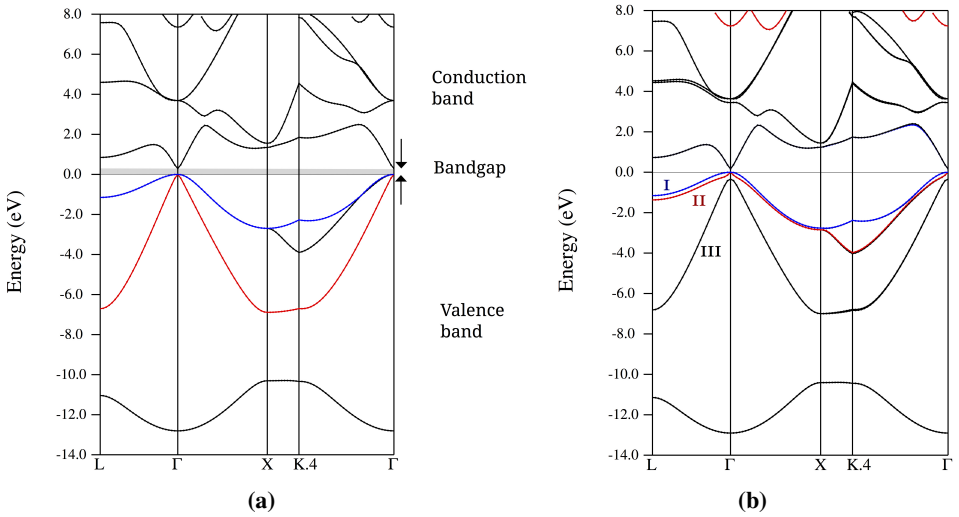

Figure 4.1:
(a): *Bandgap of GaS calculated with Wien2k without taking spin-orbit effects into account. The direct bandgap for this calculation is found to be* $E_{gap} = 0.291$ *eV. The bandgap area has been shaded and a dotted rectangle highlights the valence and conduction band edges, both appearing at* Γ. *The lowest conduction band edge is found on the lowest black band while the valence band edge appears on the red and blue bands. The conduction band and valence bands are indicated by arrows to the right.*
***(b)**: Bandgap of GaAs calculated with Wien2k including spin-orbit effects. The direct bandgap for this calculation is found to be* $E_{gap} = 0.163$ *eV. The bandgap area has been shaded and a dotted rectangle highlights the lifted degeneracy due to spin-orbit effects. (I) is called the Heavy Hole band, (II) the Light hole band and (III) the Split-Off band.*

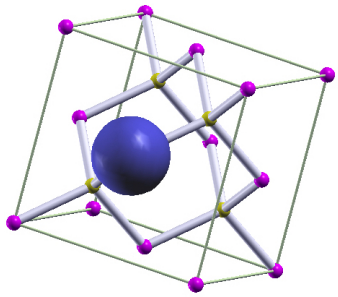

(a) s type valence band Wannier function

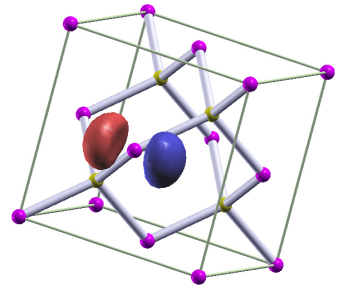

(b) p type valence band Wannier function

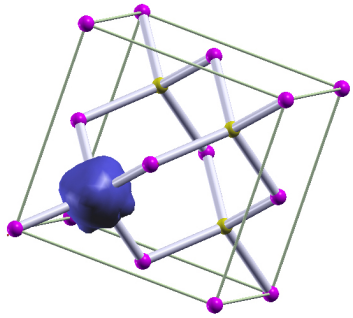

(c) s type conduction band Wannier function

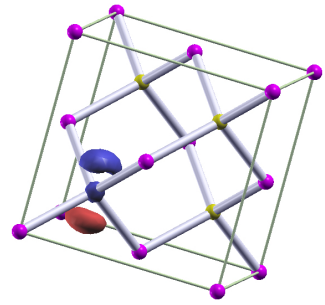

(d) s+p type conduction band Wannier function

Figure 4.2: GaAs lattice shown in the conventional unit cell. Purple bullets correspond to Ga atoms and yellow bullets represent As. **(a)**: spherically symmetric Wannier function isosurface corresponding to the lowest valence band in 4.1a. Centered around Ga atom. **(b)**: p-orbital type Wannier function isosurface corresponding to the blue and yellow bands in 4.1a. Centered around Ga atom. **(c)**: s-orbital type Wannier function isosurface corresponding to the black lowest lying conduction band in 4.1a. Spherical symmetry in the conduction band edge is characteristic for direct bandgap material. Centered around As atom. **(d)**: p and s-orbital type Wannier function isosurface corresponding to conduction band with lowest point on L (to the left in ref 4.1a).

atom, but the isosurface in this case exhibits axial symmetry characteristic of p-orbitals. The lowest conduction band state, figure 4.2c exhibits spherical symmetry. This is as expected since GaAs is a direct bandgap semiconductor. Furthermore, it is centered around an arsenide atom. For high electric field transport, the second lowest conduction band valley, occurring at L, might be relevant. As shown in figure 4.2d, this Wannier function shows mixture of both s- and p-orbitals and is centered around an arsenide atom.

4.2 Silicon

Silicon crystal is another interesting structure to test Wien2k and Wannier90 on. It differs from GaAs by having an indirect bandgap. Furthermore, it is known to have a very weak spin-orbit effect. The lattice parameter used is $a = 5.43$ Å, acquired from *crystallography.net*. The spin-orbit effect and band edge states around the bandgap of Silicon crystal are discussed here.

Calculations from Wien2k on silicon crystal are shown in figure 4.3a and 4.3b. First, the indirect bandgap nature of Si is successfully reproduced. While the conduction band edge is located near Γ in the case of GaAs, Si has its lowest conduction band valley near X. This characteristic is emphasized by a dotted rectangle in 4.3a and indirect bandgap shaded.

While the valence band edge of almost all semiconductors are described as being made up of p-orbitals, the spin-orbit effect is generally of different magnitude depending on material. In Si, the Split-Off band, analogous to the Split-Off band described for GaAs in the previous section, has been shown to be lower in energy with only $\Delta = 0.04$ eV. Including spin-orbit effects in the case of Silicon should therefore not alter the bandstructure significantly. This is indeed the case as one compares figure 4.3b which includes spin-orbit effects with the original bandstructure in figure 4.3a. There is a small lifting in the degeneracy with a black band, barely visible, appearing just below the red band, but as expected this change is very small compared to that of GaAs.
Finally, Wannier function isosurfaces for the upper valence band edge and lower conduction band edge have been plotted in 4.3a and 4.3b, respectively. The Wannier functions are plotted in the conventional cell, with light blue bullets indicating Si atoms. Due to Wien2k demanding inversion symmetry about the origin, the origin can not be taken to be at one of the Si atoms, as was done for Ga in the case of GaAs. This is why the plots from XCrysDen in the case of Si look different compared to GaAs even though they both belong to the face-centered cubic crystal structure. In figure 4.4a, it is shown that the upper valence band edge Wannier functions display axial symmetry, which is indicative of p-orbitals, as for GaAs. The next plot, an isosurface for the conduction band edge near X is shown in 4.4b. As seen in the figure, the indirect bandgap of Si results in a conduction band edge wavefunction character which is neither an s-orbital nor a p-orbital, but a mixture. This is in agreement with the behaviour of indirect bandgap materials.

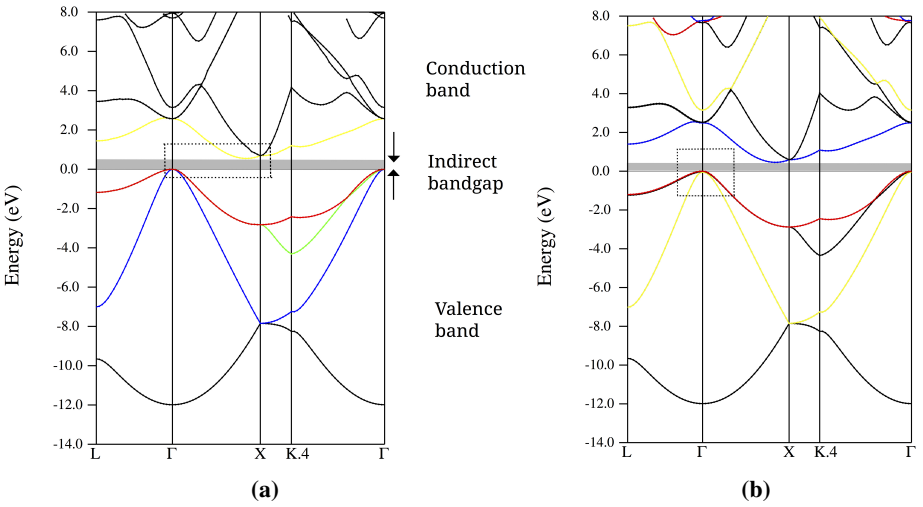

Figure 4.3:
(a): *Bandgap of Silicon calculated with Wien2k without taking spin-orbit effects into account. The indirect bandgap for this calculation is found to be* $E_{gap} = 0.484$ *eV. The bandgap area has been shaded and a dotted rectangle highlights the valence band appearing at* Γ *and conduction band edge near* X*. The lowest conduction band edge is found on the yellow band while the valence band edge appears on the red and blue bands. The conductuction band and valence bands are indicated by arrows to the right.*
(b)*: Bandgap of Silicon calculated with Wien2k including spin-orbit effects. The indirect bandgap for this calculation is found to be* $E_{gap} = 0.467$ *eV. The bandgap area has been shaded and a dotted rectangle highlights the small effect spin-orbit effects have on Si. The degeneracy in the valence band edge is barely lifted, but if one looks closely, a black band has appeared just below the red band at the valence band edge.*

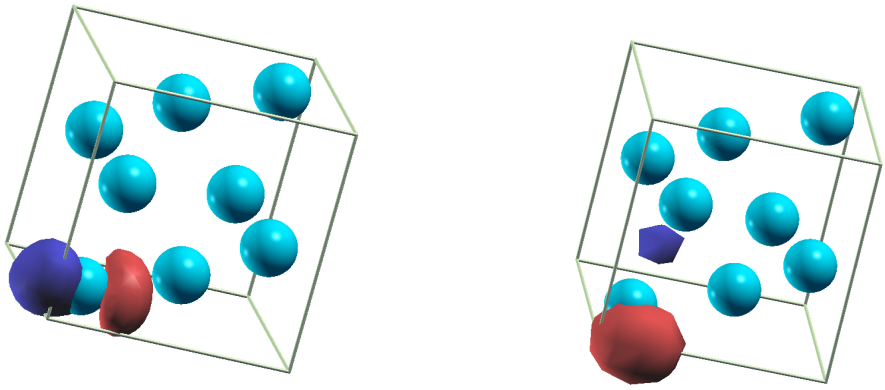

(a) p type valence band state

(b) s+p type conduction band state

Figure 4.4: **(a)**: Isosurface plotted for p-orbital type Wannier function corresponding to the red and blue bands in 4.3a. **(b)**: Isosurface plotted for s+p - orbital type Wannier function corresponding to yellow the lowest lying conduction band in 4.3a. This mixed symmetry in the conduction band edge is characteristic for indirect bandgap materials.

4.3 HgCdTe

Mercury Cadmium Telluride (MCT, CMT, HgCdTe) is a ternary alloy of CdTe and HgTe. It has a tuneable bandgap between 0 eV and 1.5 eV. The bandgap of $Hg_{0.72}Cd_{0.28}Te$ is calculated from Wien2k and discussed in light of DFT and LDA+U. A simulation with only LDA is compared to one where LDA+U has been used. To obtain a more realistic bandstructure and the correct bandgap, LDA+U allows one to better account for strongly correlated d-states. Since both simulations include spin-orbit effects, extra RLO's have been added, as explained in more detail for GaAs. The potential U was adjusted until a bandgap of $E_g = 0.212$ eV was obtained, corresponding to $Hg_{0.72}Cd_{0.28}Te$ at 80 K. This happened at $U = 35.8$ eV

The lattice parameter for $Hg_{0.72}Cd_{0.28}Te$ has been determined using Vegard's law. Vegard's law is an empirical law and states that the lattice parameter of two constituents is given by

$$a_{A_{1-x}B_x} = (1-x)a_A + xa_B \tag{4.2}$$

which yields a lattice parameter of $a_{Hg_{0.72}Cd_{0.28}Te} = 6.39$ Å. Lattice parameters used are for HgTe, $a_{HgTe} = 6.36$ Å, and for CdTe, $a_{CdTe} = 6.48$ Å. These are acquired from *crystallography.net*.

When performing spin-orbit calculations, Wien2k allows the inclusion of relativistic local orbitals (RLOs) to the eigenfunctions. These relativistic local orbitals appear as solutions to the Dirac equation, the relativistic equivalent of the Schroedinger equation, for an electron in a spherically symmetric potential. They differ from the local orbitals currently used in that all current p-orbitals used are zero at the origin while relativistic local orbitals have a finite value at the origin. Particularly for heavier elements such as Hg, the mismatch between local orbitals currently used and the behaviour of the relativistic $p_{\frac{1}{2}}$ becomes significant. [31] Thus, in both simulations of which results are shown below, RLOs have been included for all atoms.

First, a simulation for $Hg_{0.72}Cd_{0.28}Te$ including spin-orbit coupling has been performed, shown in figure 4.5a. This simulation predicts $Hg_{0.72}Cd_{0.28}Te$ to be metallic when in fact it is 0.19 eV at 0 K and increasing with temperature [35]. This underestimation of the bandgap may partly be attributed to the general issue of DFT consistently underestimating the bandgap in electronic systems [36]. There is however also a significant contribution to the underestimation of the bandgap stemming from the modelling of strongly correlated states 2.2.3. This is explained below.

For HgCdTe, the local density approximation does not provide a good model for the d-bands, so an interaction has been added to better model these states for Hg (5d) and Cd (4d). The simulation including LDA+U is shown in 4.5b. It was run with an orbital potential of $U = 35.8$ eV. It is clear that the high-lying d-bands have fallen down when one compares with the first simulation from figure 4.5a. This is caused by the additional interaction specifically added for these d-states to lower their energies. A little simplified, this

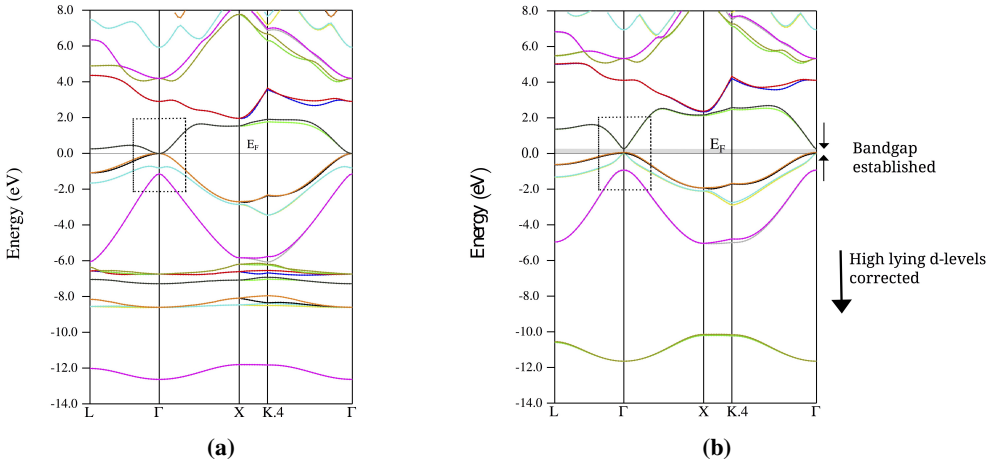

Figure 4.5: **(a)**: *Bandgap of $Hg_{0.72}Cd_{0.28}Te$ calculated with Wien2k with spin-orbit effects, but without an orbital potential U. According to experimental models, there should be a finite bandgap for this material, but this is not predicted in this calculation. The area where the bandgap should be is highlighted by a dotted rectangle.*
***(b)**: Bandgap of $Hg_{0.72}Cd_{0.28}Te$ calculated with Wien2k with spin-orbit effects and an orbital potential of $U = 35.8$ eV. The bandgap is $E_g = 0.212$ eV and corresponds to $Hg_{0.72}Cd_{0.28}Te$ at 80 K. As indicated on the figure, the high-lying d states have been adjusted downwards to establish a bandgap.*

lowering in energy may be justified as follows: strongly correlated electrons will correlate in such a way that they avoid each other as best as possible. If they consistently avoid each other through correlated movement, this corresponds to a lower energy than predicted in the local density approximation since only local correlations are taken into account in LDA.

From figure 4.5b, it is clear that thanks to the LDA+U model, a bandgap has been established. The bandgap $E_g = 0.212$ eV corresponds to $Hg_{0.72}Cd_{0.28}Te$ at 80 K. To see how LDA+U yields a bandgap, we look at its effect on the conduction band edge and valence band edge. As explained earlier, LDA+U will lower the d states in energy and consequently radially. This results in a screening of the nucleus which creates an increased negatively charged environment for states higher up than the d states. Particularly s states will, due to their general concentration near the nucleus, be sensitive to this change in electronegativity and shift upwards. On the other hand, p states which are bell curved and less concentrated near the nucleus, will be less sensitive to this screening effect. In other words, the conduction band edge, which is s type for direct bandgap materials like HgCdTe, will shift upwards to a larger degree than the valence band edge, consisting of p type states.

Even though a realistic bandgap has been obtained after adjusting for an orbital potential U, there is room for improvements. First, Wien2k supports so-called supercell structures. A

supercell is a repeating number of primitive cells where a selected number of the primitive cells may be perturbed, e.g with an impurity. A supercell of HgCdTe would offer an improvement since it is a much more realistic model for HgCdTe than Vegard's law. This perturbation of the crystal structure will at the same time perturb the electronic system in such a way that an 'unfolding' of the bandstructure is required to recover the Bloch character of electronic eigenstates [37]. A second improvement would be to replace the local density approximation currently used with mbJ, a semilocal model for the exchange-correlation potential. mbJ has been shown to capture the behaviour of orbital-dependent potentials well, and it does so at almost the same expense as LDA [38]. Using mbJ+U would therefore represent a better model than the current LDA+U.

Chapter 5

Conclusion and future work

During the work with this specialization project, a number of achievements have been made. First, the overlap integral between eigenfunctions in the LAPW function and MLWF bases have been derived. The objective has been to obtain expressions that are suitable for numerical integration over the Brillouin zone so that scattering rates for each individual scattering mechanism may be calculated. These scattering rates are needed in the carrier simulation in semiconductor materials using the Monte Carlo method. The overlap expression derived between eigenfunctions in the LAPW basis have been found good enough for the above mentioned application. On the other hand, more work remains to be done for an expression in the Wannier basis, since in this case the expression obtained was not satisfactory. In addition, calculations have been made for materials GaAs, Silicon and HgCdTe using Wien2k, Wien2Wannier and Wannier90. For GaAs, the predicted degeneracy lifting in the valence band caused by spin-orbit effects was successfully reproduced, and the eigenstates near the band edge were found to match literature data. For Si, the weak effect of spin-orbit coupling was validated, and calculated properties of the bandgap matched characteristics of Silicon's indirect bandgap. Finally, the bandstructure of $Hg_{0.72}Cd_{0.28}Te$ was calculated using LDA+U and Vegard's law. The The orbital potential U was adjusted to reach a bandgap of $E_g = 0.212$ eV, which corresponds to $Hg_{0.72}Cd_{0.28}Te$ at 80 K.

There is much that can be done to develop this work further. An applicable expression was not found for the Wannier basis, and the approximations used in the calculations of $Hg_{0.72}Cd_{0.28}Te$ are unrealistic. Suggestions for future work are therefore:

- Continue the work of finding numerically suitable expressons for scattering rates with Wannier functions.
- Use a supercell model accompanied by unfolding instead of Vegard's law for HgCdTe
- Replace the current LDA model for the exchange-correlation potential with mbJ+U.
- To generate and plot Maximally localized Wannier functions for HgCdTe.

Bibliography

[1] D. Vasileska, D. Mamaluy, H. R. Khan, K. Raleva, and S. M. Goodnick. Semiconductor device modeling. *Journal of Computational and Theoretical Nanoscience*, 5(6):999–1030, 2008.

[2] J. Singh. Electronic and optoelectronic properties of semiconductor structures. *Annals of Physics*, 54(7):258, 2003.

[3] Bjørnar Karlsen. *Calculation of phonon and alloy scattering rates in zincblende structures using 14 x 14 kp and "ab initio" pesudopotential methods*. PhD thesis, Norwegian University of Science and Technology, 2013.

[4] Jan Kuneš, Ryotaro Arita, Philipp Wissgott, Alessandro Toschi, Hiroaki Ikeda, and Karsten Held. Wien2wannier: From linearized augmented plane waves to maximally localized Wannier functions. *Computer Physics Communications*, 181(11):1888–1895, 2010.

[5] Juri Selvåg. *High Precision, Full Potential Electronic Transport Simulator: Implementation and First Results*. PhD thesis, Norwegian University of Science and Technology, 2014.

[6] Tore Sivertsen Bergslid. *Implementing a full-band Monte Carlo model for zincblende structure semiconductors*. PhD thesis, Norwegian University of Science and Technology, 2013.

[7] P Blaha, K Schwarz, and GKH Madsen. WIEN2K, An Augmented Plane Wave+ Local Orbitals Program for Calculating Crystal Properties (TU Wien, Austria, 2001). *Isbn 3-9501031-1-2*, page 2001, 2001.

[8] Nicola Marzari, Arash A. Mostofi, Jonathan R. Yates, Ivo Souza, and David Vanderbilt. Maximally localized Wannier functions: Theory and applications. *Reviews of Modern Physics*, 84(4):1419–1475, 2012.

[9] Arash A. Mostofi, Jonathan R. Yates, Young Su Lee, Ivo Souza, David Vanderbilt, and Nicola Marzari. wannier90: A tool for obtaining maximally-localised Wannier functions. *Computer Physics Communications*, 178(9):685–699, 2008.

[10] Claudia Ambrosch-Draxl and Jorge O. Sofo. Linear optical properties of solids within the full-potential linearized augmented planewave method. *Computer Physics Communications*, 175(1):1–14, 2006.

[11] Xinguo Ren, Patrick Rinke, Christian Joas, and Matthias Scheffler. Random-phase approximation and its applications in computational chemistry and materials science. *Journal of Materials Science*, 47(21):7447–7471, 2012.

[12] G. Kotliar, S. Y. Savrasov, K. Haule, V. S. Oudovenko, O. Parcollet, and C. A. Marianetti. Electronic structure calculations with dynamical mean-field theory. *Reviews of Modern Physics*, 78(3):865–951, 2006.

[13] E. Assmann, P. Wissgott, J. Kuneš, A. Toschi, P. Blaha, and K. Held. Woptic: Optical conductivity with Wannier functions and adaptive k-mesh refinement, 2015.

[14] B. K. Ridley. *Quantum processes in semiconductors*. Oxford University Press, 1999.

[15] G. K H Madsen and David J. Singh. BoltzTraP. A code for calculating band-structure dependent quantities. *Computer Physics Communications*, 175(1):67–71, 2006.

[16] K. Durczewski and M. Ausloos. Nontrivial behavior of the thermoelectric power: Electron-electron versus electron-phonon scattering. *Physical Review B*, 61(8):5303–5310, 2000.

[17] Giovanni Pizzi, Dmitri Volja, Boris Kozinsky, Marco Fornari, and Nicola Marzari. BoltzWann: A code for the evaluation of thermoelectric and electronic transport properties with a maximally-localized Wannier functions basis. *Computer Physics Communications*, 185(1):422–429, 2014.

[18] G. Gilat and L. J. Raubenheimer. Accurate Numerical Method for Calculating Frequency Distribution Functions in Solids. *Physical Review*, 147(2):670–670, 1966.

[19] Massimo Fischetti and Steven Laux. Monte carlo analysis of electron transport in small semiconductor devices including band-structure and space-charge effects. *Physical Review B*, 38(14):9721–9745, 1988.

[20] Warren E. Pickett, Henry Krakauer, and Philip B. Allen. Smooth Fourier interpolation of periodic functions. *Physical Review B*, 38(4):2721–2726, 1988.

[21] Einar Halvorsen. *Numerical calculation of valence band and hole scattering rates in GaAs*. PhD thesis, Norges Tekniske Høgskole, 1991.

[22] T. Brudevoll, T. A. Fjeldly, J. Baek, and M. S. Shur. Scattering rates for holes near the valence-band edge in semiconductors. *Journal of Applied Physics*, 67(12):7373–7382, 1990.

[23] W. Kohn and L. J. Sham. Self-consistent equations including exchange and correlation effects. *Physical Review*, 140(4A), 1965.

[24] H. Eschrig and W.E. Pickett. Density functional theory of magnetic systems revisited. *Solid State Communications*, 118(3):123–127, 2001.

[25] Burak Himmetoglu, Andrea Floris, Stefano De Gironcoli, and Matteo Cococcioni. Hubbard-corrected DFT energy functionals: The LDA+U description of correlated systems. *International Journal of Quantum Chemistry*, 114(1):14–49, 2014.

[26] Hal Tasaki. The Hubbard model - an introduction and selected rigorous results. *Journal of Physics: Condensed Matter*, 10(20):4353, 1998.

[27] Vladimir I. Anisimov, Jan Zaanen, and Ole K. Andersen. Band theory and Mott insulators: Hubbard U instead of Stoner I. *Physical Review B*, 44(3):943–954, 1991.

[28] V. I. Anisimov, I. V. Solovyev, M. A. Korotin, M. T. Czyyk, and G. A. Sawatzky. Density-functional theory and NiO photoemission spectra. *Physical Review B*, 48(23):16929–16934, 1993.

[29] Karlheinz Schwarz. DFT calculations of solids with LAPW and WIEN2k. *Journal of Solid State Chemistry*, 176(2):319–328, 2003.

[30] K. Schwarz, P. Blaha, and G. K H Madsen. Electronic structure calculations of solids using the WIEN2k package for material sciences. *Computer Physics Communications*, 147(1-2):71–76, 2002.

[31] David J. Singh and Lars Nordstrom. *Planewaves, pseudopotentials and the LAPW method: Second edition*. Springer, 2006.

[32] Georg K. H. Madsen, Peter Blaha, Karlheinz Schwarz, Elisabeth Sjöstedt, and Lars Nordström. Efficient linearization of the augmented plane-wave method. *Physical Review B*, 64(19):1–9, 2001.

[33] E. I. Blount. Formalisms of Band Theory. *Solid State Physics - Advances in Research and Applications*, 13(C):305–373, 1962.

[34] H Monkhorst and J Pack. Special points for Brillouin zone integrations. *Physical Review B*, 13(12):5188–5192, 1976.

[35] Junhao Chu, Shichou Xu, and Dingyuan Tang. Energy gap versus alloy composition and temperature in Hg1-xCdxTe. *Applied Physics Letters*, 43(11):1064–1066, 1983.

[36] John P Perdew. Density functional theory and the band gap problem. *International Journal of Quantum Chemistry*, 28(S19):497–523, 2009.

[37] O. Rubel, A. Bokhanchuk, S. J. Ahmed, and E. Assmann. Unfolding the band structure of disordered solids: From bound states to high-mobility Kane fermions. *Physical Review B - Condensed Matter and Materials Physics*, 90(11), 2014.

[38] Fabien Tran and Peter Blaha. Accurate band gaps of semiconductors and insulators with a semilocal exchange-correlation potential. *Physical Review Letters*, 102(22), 2009.